DOT/FAA/TC-17/22

Federal Aviation Administration
William J. Hughes Technical Center
Aviation Research Division
Atlantic City International Airport
New Jersey 08405

Effect of Ice Accretion on Full-Scale, Swept-Wing, Aerodynamic Performance and Control Effects

May 2018

Final Report

U.S. Department of Transportation
Federal Aviation Administration

NOTICE

Technical Report Documentation Page

1. Report No.
DOT/FAA/TC-17/22

2. Government Accession No.

3. Recipient's Catalog No.

4. Title and Subtitle
Effect of Ice Accretion on Full-Scale, Swept-Wing, Aerodynamic Performance and Control Effects

5. Report Date
May 2018

6. Performing Organization Code

7. Author(s)
Jeff M. Diebold[1], Brian S. Woodard[1], Stephanie Camello[2], and Michael B. Bragg[2]

8. Performing Organization Report No.

9. Performing Organization Name and Address

[1]University of Illinois at Urbana-Champaign
306 Talbot Laboratory, MC-236
104 S. Wright St
Urbana, IL 61801

[2]University of Washington – College of Engineering
371 Loew Hall
3920 E. Stevens Way NE
Seattle, WA 98195

10. Work Unit No. (TRAIS)

11. Contract or Grant No.

12. Sponsoring Agency Name and Address

U.S. Department of Transportation
FAA Northwest Mountain Regional Office
1601 Lind Ave SW
Renton, WA 98057

13. Type of Report and Period Covered
Final Report

14. Sponsoring Agency Code
ANM-112

15. Supplementary Notes
The FAA William J. Hughes Technical Center Aviation Research Division COR was Jim Riley.

16. Abstract

This report summarizes the work done under this grant at the University of Illinois. This includes the development of a classification system for swept-wing ice accretions based on the flowfield and aerodynamic impact of the ice. This is followed by a discussion of a laser scanner technique used to create high-fidelity digital representations of ice accretions for use in aerodynamic testing. The baseline swept-wing geometry for this program is then described, followed by a detailed discussion of the experimental aerodynamics work conducted at the University of Illinois. This work includes low-Reynolds number wind-tunnel tests designed to investigate and develop experimental techniques that can be used for the investigation of iced swept-wing flowfield and aerodynamics. The report concludes with a discussion of the methodology used for the development of high-fidelity artificial ice shapes for low- to high-Reynolds number experiments.

17. Key Words
Swept-wing icing, Inflight icing, Icing wind tunnel, Swept-wing ice shapes, Swept-wing model, Icing simulation, Swept-wing flowfield, 3D wing icing

18. Distribution Statement
This document is available to the U.S. public through the National Technical Information Service (NTIS), Springfield, Virginia 22161. This document is also available from the Federal Aviation Administration William J. Hughes Technical Center at actlibrary.tc.faa.gov.

19. Security Classif. (of this report)
Unclassified

20. Security Classif. (of this page)
Unclassified

21. No. of Pages
60

22. Price

Form DOT F 1700.7 (8-72) Reproduction of completed page authorized

ACKNOWLEDGEMENTS

This work was funded by the FAA Office of Aviation Research. At the University of Illinois, the authors were supported under FAA grant DOT FAA 10-G-004 with Dr. James T. Riley as the contracting officer's representative.

TABLE OF CONTENTS

LIST OF FIGURES

LIST OF TABLES

LIST OF SYMBOLS AND ACRONYMS

α	Angle of attack
α_{stall}	Stalling angle of attack
c	Chord
C_d	Local total drag coefficient
C_{di}	Local induced drag coefficient
C_{dp}	Local profile drag coefficient
C_D	Wing total drag coefficient
C_{Di}	Wing induced drag coefficient
$C_{D,min}$	Wing minimum total drag coefficient
C_{Dp}	Wing profile drag coefficient
C_l	Local lift coefficient
C_L	Wing lift coefficient
$C_{L,stall}$	Wing lift coefficient at α_{stall}
c_{LE}	Leading-edge length of splitter plate leading –edge components
C_M	Wing pitching moment coefficient
C_p	Pressure coefficient
δ_{99}	Boundary layer height at $U/U\infty = 0.99$
U	Streamwise velocity
U_∞	Freestream velocity
2y/b	Nondimensional spanwise location
5HP	Five-hole probe
AR	Aspect ratio
CAD	Computer-aided design
CCD	Charge-coupled device
CRM	Common Research Model
FR5HP	Fast response five-hole probe
IPS	Ice-protection system
IRT	Icing Research Tunnel
PSP	Pressure-sensitive paint
RPM	Rapid prototype manufacturing
SLA	Stereolithography
UIUC	University of Illinois at Urbana Champaign

EXECUTIVE SUMMARY

This report presents the results of work performed at the University of Illinois as part of a program designed to improve our understanding of iced swept-wing aerodynamics. Accomplishments include the development of a swept-wing ice-accretion classification system. The classifications are based on the fundamental flowfield generated by the ice accretion rather than the formation process of the ice. This report also discusses a laser-scanning method that will be used to create digital representations of ice accretions formed in the Icing Research Tunnel. Wind-tunnel testing was performed at the University of Illinois 3-by-4-ft Low-Speed Wind Tunnel to evaluate this laser scanning technique, comparing the aerodynamic performance of a model with artificial ice shapes made using laser scanning to the traditional mold and casting process. The testing showed that the two processes resulted in artificial ice shapes that had closely matched aerodynamic performance effects. Most of this report focuses on a series of wind-tunnel studies conducted at the University of Illinois to gain experience in testing swept wings with leading-edge ice and to investigate and further develop various experimental techniques to improve understanding of the complicated aerodynamics involved in swept-wing icing. The baseline swept-wing model for the program is a 65% scale version of the Common Research Model, designated CRM65. A small-scale model derived from the baseline model was constructed for use in the 3-by-4 Low-Speed Wind Tunnel at the University of Illinois. The model was designed with a removable leading edge so that a simulated ice shape could be tested.

Force-balance measurements, surface-pressure measurements, and surface-oil flow visualization were used to compare aerodynamic and flow characteristics of the model with a clean and iced leading edge at Reynolds numbers of 3×10^5, 6×10^5, and 7.8×10^5. Force-balance measurements indicated a significant performance penalty resulting from the leading-edge ice shape. Surface-pressure measurements and surface oil flow visualization indicated the performance penalties were the result of a spanwise running leading-edge vortex that formed behind the ice shape. This vortex increased in size as the angle of attack of the wing increased until the flow failed to reattach over the outboard sections of the wing. The vortex was then shed into the wake.

Advanced experimental techniques were investigated to determine their value in studying swept-wing icing. The method selected for further development is the five-hole probe wake-survey technique. Wake-survey results from the 3-by-4 Low-Speed Wind Tunnel are presented. These results indicate a significant increase in profile drag due to the leading-edge ice shape and complex spanwise distributions of lift and drag on the iced swept wing. A series of experiments was conducted to investigate how splitter-plate geometry influences the flow over the splitter plate. Results from these experiments are being used to design a splitter plate for the planned experiments in larger wind tunnels. The report concludes with a discussion of the process that will be used to generate artificial ice shapes for future wind-tunnel tests.

1. INTRODUCTION

Airframe icing continues to present challenges to aircraft designers and manufacturers. The accretion of ice, especially on lifting surfaces, can have a significant impact on an aircraft; even small ice accretions can lead to a decrease in maximum lift and stall angle, an increase in drag, and degradation of control authority. There is a significant amount of research detailing the aerodynamic effects of ice accretions on 2D airfoils [1, 2]. Systematic experimental studies have been performed that have provided information about the aerodynamic performance, control, and flowfield of iced airfoils. The aerodynamic effects of airfoil geometry and ice-accretion geometry are generally understood, including size and location of the ice shape. The flowfield and the underlying physics that drive performance degradations have also been extensively studied. A series of low- [3] and high-Reynolds [4] number experiments have addressed the influence of ice-shape-simulation fidelity and Reynolds number effects.

In contrast, study of the aerodynamics of 3D swept wings with ice has been very limited. Swept-wing icing presents a challenging problem because of the large number of variables involved and the complexity of the flow. Several geometric features must be considered, including sweep angle, aspect ratio, taper ratio, twist, and changes in airfoil geometry along the span. Spanwise variation in the ice accretion must also be considered.

Although research has been limited, there have been several experimental studies of the aerodynamics and flowfields of swept wings with ice. Khodadoust and Bragg [5] and Bragg et al. [6] used pressure measurements, surface oil flow, helium-bubble flow visualization, and laser-Doppler velocimeter measurements to study the flowfield of an iced swept wing with NACA 0012 airfoil section. The experimental results showed that the flowfield was dominated by a leading-edge vortex that grew as the angle of attack increased and was shed into the wake as the wing stalled. Papadakis et al. [7, 8] examined the performance degradation of a swept wing with high-fidelity castings of complex 3D ice accretions and simplified artificial ice accretions.

The majority of studies in the literature were performed at low-Reynolds number and used simplified swept-wing geometries or simplified artificial ice shapes. To advance our understanding of 3D iced swept-wing aerodynamics, it is necessary to conduct a study that includes high-Reynolds number experimental studies and high-fidelity artificial ice shapes. Over the past several years, the University of Illinois, under a grant from the FAA and in collaboration with NASA Glenn Research Center, conducted research in preparation for meeting this goal. Specific goals of the research effort include:

- Classifying ice accretion shapes on 3D wings based on flowfield and aerodynamic effects.
- Developing a systematic understanding of the aerodynamic effect of icing on swept wings, including: Reynolds and Mach number effects, important flowfield physics, and fundamental differences from 2D.
- Determining the level of ice-shape geometric fidelity required for accurate aerodynamic simulation of swept-wing icing effects.

This report summarizes the work done under this grant at the University of Illinois. This includes the development of a classification system for swept-wing ice accretions based on the flowfield and aerodynamic impact of the ice. This is followed by a discussion of a laser-scanner technique used to create high-fidelity digital representations of ice accretions for use in aerodynamic testing. The baseline swept-wing geometry for this program is then described, followed by a detailed discussion of the experimental aerodynamics work conducted at the University of Illinois. This work includes low-Reynolds-number wind-tunnel tests designed to investigate and develop experimental techniques that can be used for the investigation of iced swept-wing flowfield and aerodynamics. The report concludes with a discussion of the methodology used for the development of high-fidelity artificial ice shapes for low- to high-Reynolds number experiments.

2. SWEPT-WING ICING CLASSIFICATION

The accretion of ice on an aircraft in flight is affected by many factors, including atmospheric conditions, geometry of the aircraft, and local aerodynamics. It is common for the ice accretion to be classified based on its appearance or composition, which depends on the accretion thermodynamics. The ice can then be described as glaze, rime, mixed, or runback ice. Although this terminology is valuable in many contexts, it may not be useful when trying to understand the aerodynamic effects of the ice. This is because the aerodynamics are influenced by the geometric features of the ice rather than its composition. In the case of airfoil icing, Bragg et al. [1] developed four ice-accretion classifications based on the flowfield physics unique to each category. This categorization provided a framework for quantifying the effects of ice-shape geometric fidelity on ice-airfoil aerodynamics. Because of the usefulness of the classification system for airfoil icing research, it was determined that a similar classification system for swept-wing icing would be valuable. In the early stages of this grant, a swept-wing ice accretion classification system and a review of the current swept-wing icing literature was developed and documented by Broeren et al. [9] and Diebold et al. [10]. The four classifications are roughness, streamwise ice, spanwise-ridge ice, and horn ice. These categories are briefly summarized here.

Regardless of the icing conditions, the initial stages of in-flight icing involve the formation of small-scale roughness on the surface of the wing. From an aerodynamics point of view, a key feature of the roughness is that it is usually much larger than the boundary-layer thickness. An individual roughness element generates a complex 3D flowfield in which the scale of the separated region is of the same order as the size of the roughness. On an aerodynamic surface, a distribution of roughness elements forms. The distribution can be characterized by the roughness height, concentration, and chordwise extent on the surface. Roughness influences the aerodynamics by inducing boundary-layer transition, which increases skin-friction drag and extracting momentum from the boundary promoting trailing-edge separation. Fundamentally, the characteristics of ice roughness on swept wings are nearly the same as roughness on airfoils and straight wings. A primary difference is that on an airfoil or straight wing, there is a small zone of smooth ice near the stagnation point, whereas on a swept wing, the ice near the attachment line may exhibit roughness due to the spanwise flow.

In rime icing conditions, it is common for the initial roughness to develop with time into streamwise ice. In these conditions, the water droplets freeze immediately after impinging on the wing, resulting in a shape that tends to conform to the leading edge. Flow separation can occur because of discontinuities in the geometry, but the scale of the separated flow is usually small. In general, streamwise ice has a limited adverse impact on the aerodynamics. The effects of streamwise ice on the aerodynamics of swept wings have received very little attention in the literature.

The spanwise-ridge ice can form in a number of different icing conditions and is characterized by a ridge of ice downstream of the leading edge of the surface, often in the range of 10%–15% of the chord, whereas the leading edge is relatively free of ice. Spanwise-ridge ice sometimes occurs downstream of an area covered by an ice-protection system (IPS) that does not completely evaporate the water or for which drops impinge downstream of the IPS. The ridge acts as a fence or flow obstacle and can exhibit substantial spanwise variation in geometry. Like streamwise ice, there is little in the literature regarding the effects of spanwise-ridge ice on the aerodynamics of swept wings. On airfoils, the primary feature of the spanwise-ridge flowfield is a complex and unsteady separated flow region downstream of the ridge. The effects of the spanwise-ridge have been shown to be sensitive to the airfoil pressure distribution and other important features, including the ridge geometry, size, and location [1].

The final classification is horn ice, which has received the most attention in the swept-wing icing literature. Horn ice refers to a large protuberance at the leading edge of the wing or airfoil and is characterized by its height, the angle it makes with the surface, and the location on the surface. The flowfield is dominated by a large separated region behind the ice shape. On an airfoil prior to stall, the separated flow reattaches, forming a separation bubble, which can cover as much as 50% of the chord before complete separation. Because of spanwise flow on a swept wing, the flow may reattach to form a spanwise running leading-edge vortex similar to the leading-edge vortex on a delta wing. As the angle of attack of the wing increases, the chordwise extent of the vortex increases until it finally sheds from the outboard section of the wing, resulting in stall.

On an airfoil, the horn ice exhibits, at most, small-scale spanwise variation in the geometry, but this is not necessarily true on a swept wing. When the sweep angle is increased, the horn ice may exhibit highly 3D features commonly referred to as scallops. As can be seen in figure 1, the scalloped ice shape can have significant variation in geometry over a short spanwise distance. From an ice-accretion perspective, the horn ice can be subdivided into “complete scallops,” “incomplete scallops,” and “no scallops” [11]. The no-scallops case is just a standard horn ice. Currently, only one study has measured the aerodynamic impact of scalloped ice shapes on swept wings [12]. Although this study did not include detailed flowfield measurements, the data suggest that, from an aerodynamic standpoint, the ice accretion of “no scallops” and “incomplete scallops” is very similar, whereas the “complete scallops” exhibits a different flowfield. As a result, the classification of horn ice for a swept wing is subdivided into “nominally 3D” and “highly 3D” horn ice. The nominally 3D horn ice includes the cases of no scallops and incomplete scallops, whereas highly 3D refers to complete scallops.

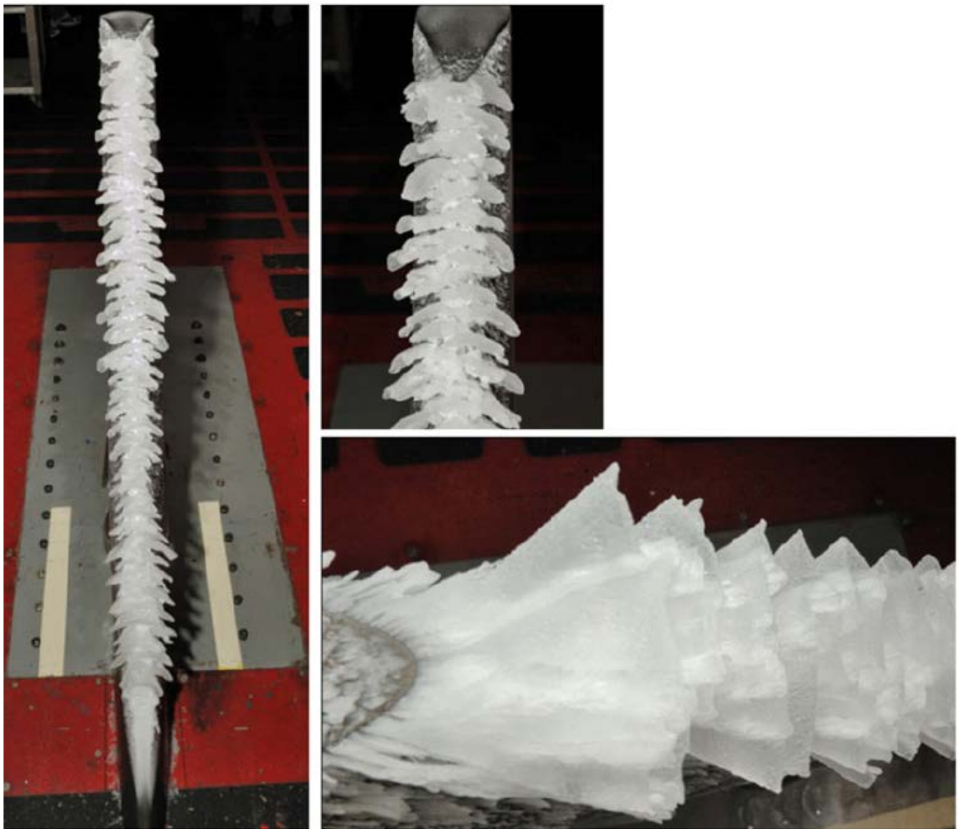

Figure 1. Photograph of complete scallop ice shape on a swept NACA 0012

During development of the swept-wing icing classification system, the swept-wing icing literature was sparse compared to the airfoil icing literature. Only a small number of studies have investigated the flowfield of swept wings with ice in any detail. It is, therefore, possible that as more data are available, this classification system may require updating.

3. LASER SCANNER VALIDATION

Most experimental data on the effects of ice on airfoil and wing aerodynamics have been obtained by testing models with artificial ice shapes in dry-air wind tunnels. An important step required for these experiments is the acquisition, documentation, and production of ice-shape geometries for testing on the models. The geometric representation of the ice accretion used in the wind tunnel is typically referred to as an “artificial ice shape” or an “ice-accretion simulation” [13]. The term “artificial ice shape” is used in this report. Traditionally, high fidelity artificial ice shapes have been obtained by creating a mold of an ice accretion from an icing wind tunnel and then creating a casting from the mold [13, 14]. Limitations of the mold and casting method include the time and labor involved and the lack of a digital representation of the 3D geometry. In the Swept-Wing Icing Program, separate artificial ice shapes for models of three sections of the complete swept-wing model will be obtained in NASA’s Icing Research Tunnel (IRT), using 3D swept hybrid wing section models designed by Fujiwara et al. [15]. The resulting high-fidelity artificial ice shapes for the three sections then must be blended together to form a full-span artificial ice shape, and then scaled to the correct size for the aerodynamic model. This could not be accomplished using the traditional mold and casting procedure because it requires digital representations of the ice accretion that can be manipulated to obtain a full span, subscale model for testing in a dry-air, aerodynamic wind tunnel.

Engineers at NASA’s Glenn Research Center have recently developed a 3D laser scanner method to acquire digital representations of ice accretions. Artificial ice shapes can be constructed from the digital representations using rapid prototype manufacturing (RPM) methods, and these shapes can then be installed on a model and used in aerodynamic testing [16]. University of Illinois at Urbana Champaign (UIUC) performed tests and analyses to determine if ice shapes obtained from the digital scanning, RPM method provided comparable aerodynamic results to those obtained from the mold and casting method. Several wind-tunnel tests were conducted in the 3-by-4 Low-Speed Wind Tunnel at the University of Illinois to assess the aerodynamic accuracy of ice-accretion simulations generated from the laser scan [17, 18]. Several different types of ice accretions were generated in the IRT on a 2D NACA 23012 airfoil model. For each ice accretion, a laser scan was performed, followed by the molding process. The laser scan was used to generate a 3D ice-accretion simulation using RPM, and the mold was used to create a casting. This allowed direct aerodynamic comparison of the two methods. These ice-accretion simulations were instrumented with pressure taps and fit onto the leading edge of a NACA 23012 airfoil model in the wind tunnel. Aerodynamic performance testing was carried out at a Reynolds number of 1.8×10^6.

The agreement of performance data and surface pressures was excellent between the casting and RPM simulations for the majority of the ice-accretions simulations tested. The geometries included a roughness, streamwise, and spanwise-ridge ice accretion. Figure 2 compares the aerodynamic performance data of the RPM and casting simulations for a streamwise ice accretion. The agreement in lift, drag, and pitching moment is excellent. Of the six cases tested, two exhibited poor comparison. One was a rime-ice roughness accretion. The roughness heights of this accretion were estimated to be smaller than the measurement accuracy of the laser scanner and the manufacturing capabilities of the rapid prototyping method explaining the poor comparison. The second ice accretion that exhibited poor comparison between the two methods was the horn ice case. It was clear from a visual inspection of the horn ice formed with the two simulation methods that the horn of the casting was smaller and more rounded than the horn of the RPM simulation. This was attributed to shrinkage and warpage of the casting [16]. This theory was validated by performing a laser scan of the casting of this horn ice. A comparison of the aerodynamic performance of the horn ice casting and the laser scan of this casting showed excellent agreement. This indicates that the laser-scan method, at least in this case (the assumption is that it does in general), provides a more accurate representation of the ice-accretion geometry. The laser scan technology will play a key role in the development of ice-accretion simulations for the current swept-wing icing program.

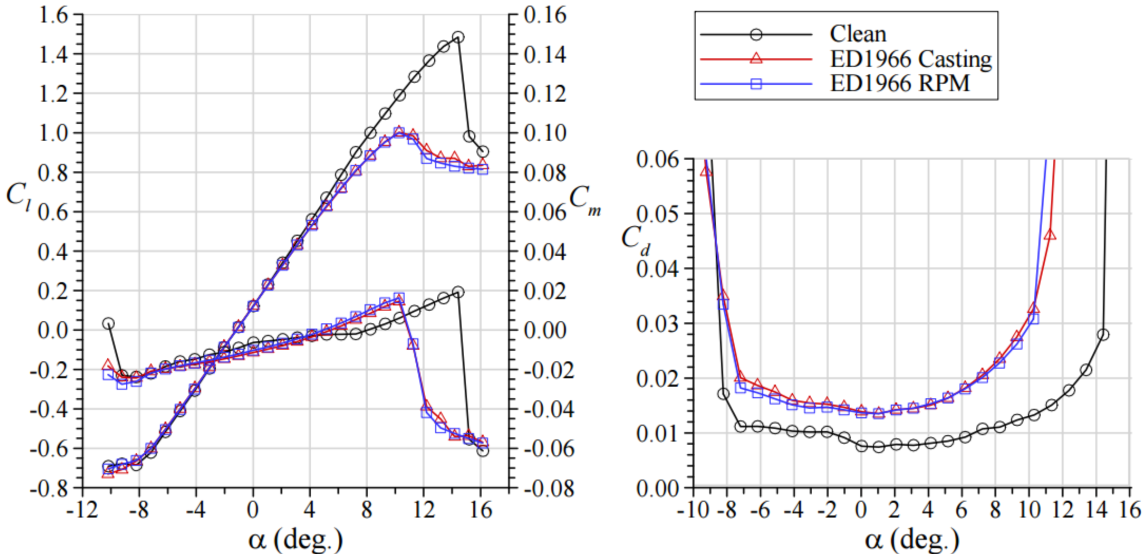

Figure 2. Aerodynamic performance comparison for streamwise ice-shape casting and RPM simulations on the NACA 23012 Airfoil at Re = 1.8×106 and M = 0.18

4. CRM SWEPT WING

An important early step in the current swept-wing icing program was the selection of a swept-wing geometry. The goal was to select a baseline geometry that would be representative of modern civilian transport airplanes. It was also important that the geometry be nonproprietary and non-export controlled. The Common Research Model [19] (CRM) developed by The Boeing Company and NASA satisfied the necessary criteria. The CRM is representative of a wide-body transport airplane similar to a Boeing 777 or Airbus A330. The wing has a quarter chord sweep angle of 35 degrees, uses a modern transonic supercritical airfoil, and is designed to be well behaved with and without the engine nacelle/pylon. A significant advantage of the CRM is that all of the geometry information, CFD analysis, and experimental results are in the public domain. Whereas the CRM was designed as a complete aircraft with fuselage, tail, and engine nacelle/pylons, the current swept-wing icing program will only use the semispan wing without the engine.

The CRM is very large compared to other swept-wing airplanes, such as single-aisle commercial transports used as regional and business jets. The large size of the CRM presents significant challenges to both the ice-accretion and aerodynamic testing. These challenges result from the large-scale reduction that would be necessary to use this geometry in the IRT and the wind tunnel used for aerodynamic testing. This scaling would make it difficult to accurately reproduce the small roughness found on most ice accretions. Because of this challenge, it was decided that the baseline geometry for the swept-wing icing program would be a 65% scale version of the CRM. This will be referred to as CRM65. Figure 3 summarizes the geometry of CRM65. In addition to scaling the CRM, the dihedral was also removed.

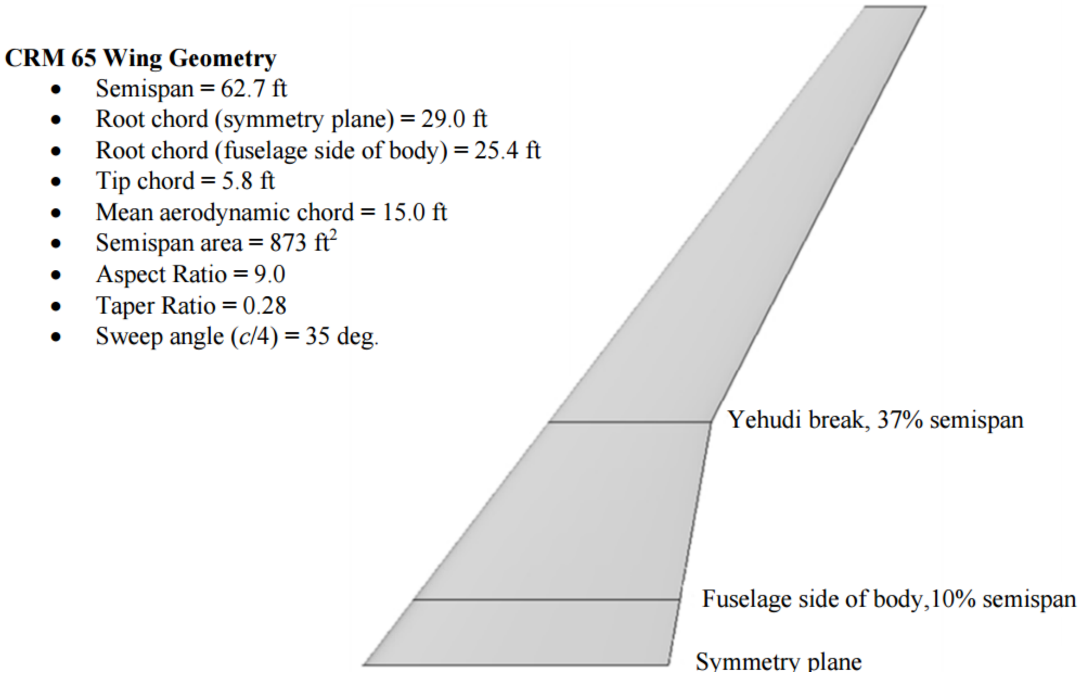

CRM 65 Wing Geometry

- Semispan = 62.7 ft
- Root chord (symmetry plane) = 29.0 ft
- Root chord (fuselage side of body) = 25.4 ft
- Tip chord = 5.8 ft
- Mean aerodynamic chord = 15.0 ft
- Semispan area = 873 ft^2
- Aspect Ratio = 9.0
- Taper Ratio = 0.28
- Sweep angle ($c/4$) = 35 deg.

Figure 3. Summary of CRM65 wing geometric characteristics

5. DEVELOPMENT OF DIAGNOSTICS FOR SWEPT WINGS WITH ICE ACCRETIONS

5.1 OVERVIEW

The swept-wing research program will include numerous wind-tunnel tests in several facilities. At this stage in the program, the majority of the wind-tunnel tests have been performed at the University of Illinois's 3-by-4 Low-Speed Wind Tunnel. The primary goal of these experiments has been to gain experience testing swept wings with leading-edge ice simulations and to develop experimental techniques that can improve our understanding of swept-wing icing aerodynamics and performance. This section will discuss the swept-wing model used at UIUC and the important results obtained from these experiments.

5.2 UNIVERSITY OF ILLINOIS SWEPT WING MODEL

It was necessary to design and build a semispan swept-wing model for the UIUC wind tunnel prior to performing these experiments. Because of the very low Reynolds number that could be achieved in the 3-by-4 wind tunnel, the data acquired in the facility are likely not representative of the aircraft in flight. Because the goal of the UIUC tests was to develop experimental techniques, it was determined that modifications could be made to the CRM geometry without comprising the experiments. The CRM geometry was modified in several ways to improve the strength of the small-scale model and to reduce the complexity and cost. Modifications included removing the dihedral, linearizing the spanwise twist distribution, increasing the thickness by 20% around the camber line, and increasing the trailing-edge thickness. The geometry of the UIUC model is summarized in table 1.

Table 1. UIUC Wind-tunnel model geometry

Span (ft)	Wing Area (ft^2)	AR	c/4 Sweep (deg)	Taper	Mean Aero Chord (ft)
2.1	1.0625	8.3	35	0.296	0.5167

The design of the model included an internal steel frame for structural support and an outer shell to provide the aerodynamic surface. The outer shell was manufactured using the rapid-prototype process stereolithography, and consisted of three components: a lower surface, an upper surface, and a leading edge. The complete model is shown mounted in the tunnel in figure 4. The steel frame of the model passed through the floor of the wind tunnel to mount directly to the force balance. The model also contained five rows of pressure taps oriented parallel to the freestream. The spanwise locations of the pressure taps are shown in table 2. The leading edge of the model was designed to be removable so the model could be tested with either a clean or iced leading edge. A simple ice-shape simulation was developed using NASA’s LEWICE 2D program. The ice-shape simulation used several 2D ice accretions blended together along the span of the model. Figure 5 shows the cross section of the ice shape at several spanwise locations. Note that the axes in figure 5 are normalized by the local chord. The size of the ice shape relative to the local chord increases toward the tip. More details about the model and ice shape can be found in Diebold [20] and Diebold et al. [21].

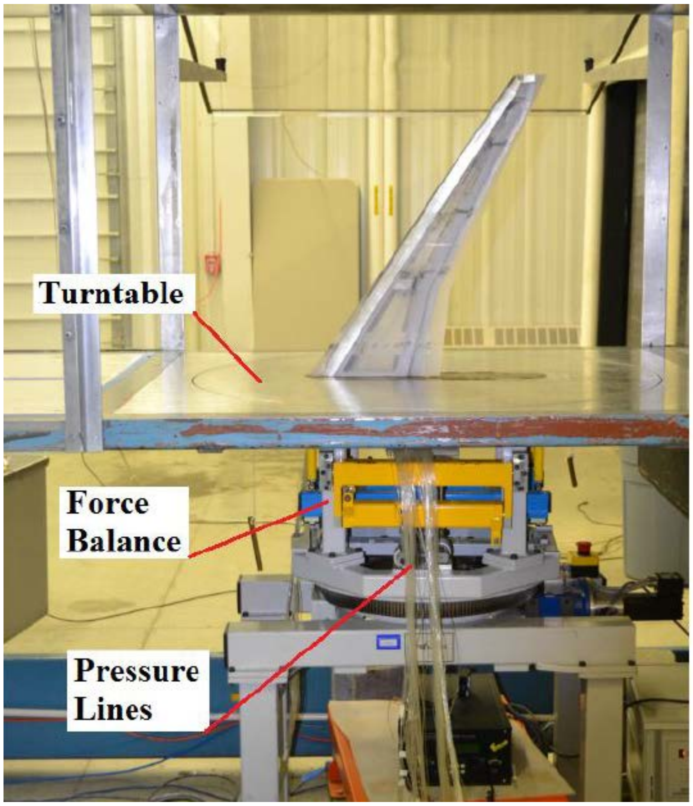

Figure 4. The UIUC wind-tunnel model mounted in the wind tunnel

Table 2. Spanwise location of pressure taps on UIUC model

Row	2y/b
1	0.11
2	0.36
3	0.55
4	0.77
5	0.92

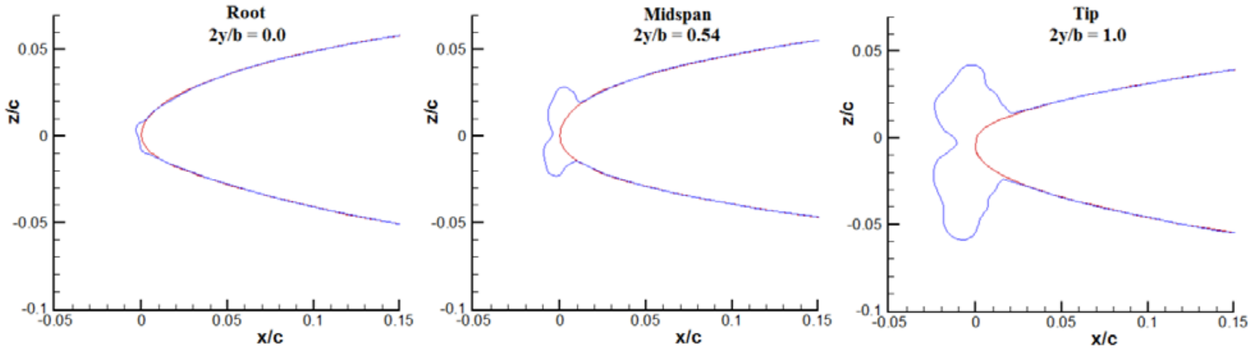

Figure 5. Ice shape cross-section at several spanwise locations on the UIUC model

5.3 AERODYNAMIC AND SURFACE-PRESSURE MEASUREMENTS

This section presents aerodynamic performance data and surface-pressure measurements obtained in the UIUC wind tunnel. Force-balance measurements for the clean and iced wing over a range of Reynolds numbers are shown in figure 6. The Reynolds number was based on the freestream velocity and the mean aerodynamic chord. The influence of the ice on the aerodynamic performance was significant. The average increase in C_{Dmin} due to the ice shape was 78.7% with a maximum of 85.8% occurring at Re = $3x10^5$ over the tested Reynolds number range. The average increase in drag of the iced wing was 58.3% with a maximum increase of 68% occurring at RE = $3x10^5$ at a lift coefficient of 0.5.

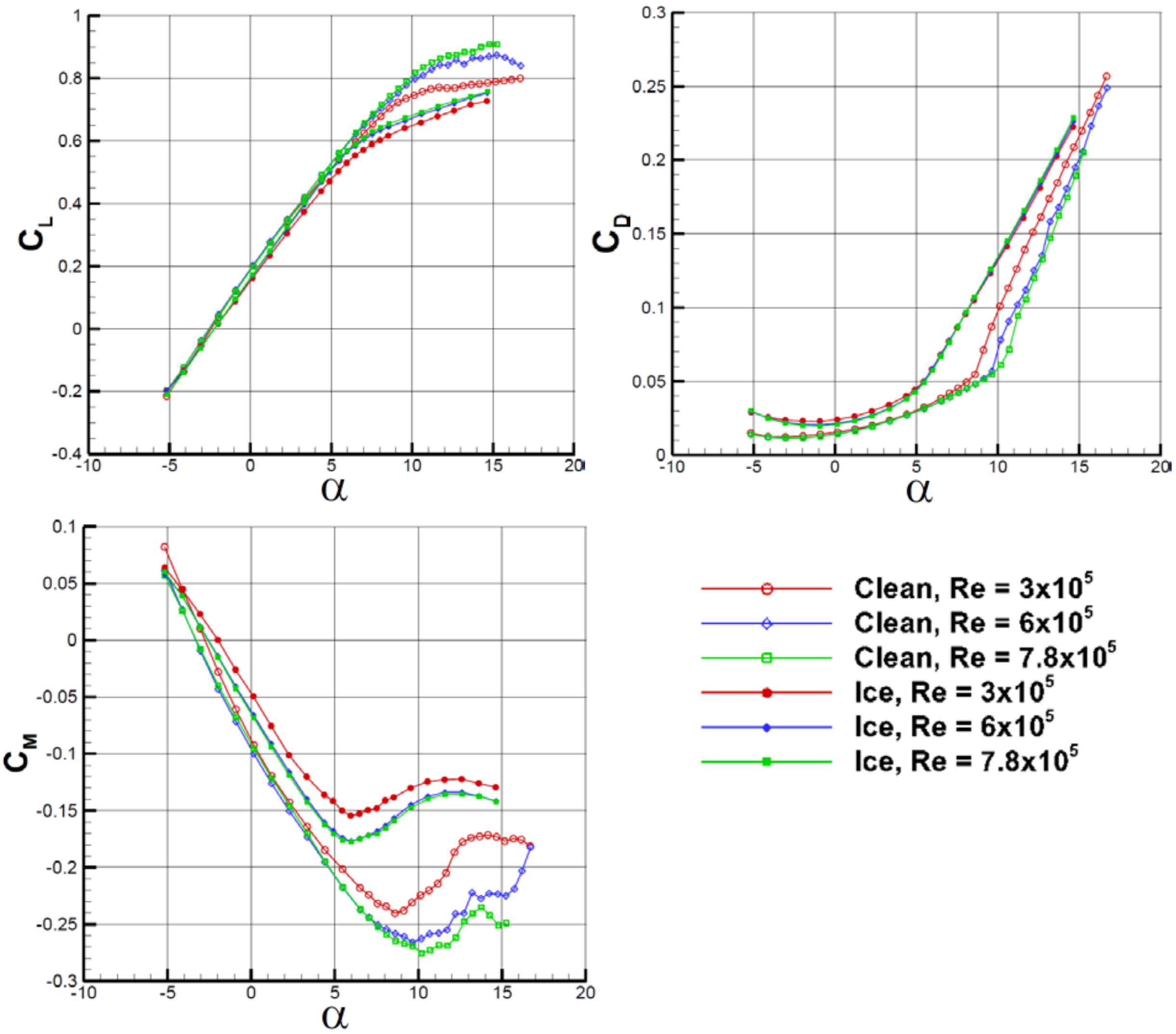

Figure 6. The UIUC force-balance results

The stalling characteristics of the wing can be inferred from the balance data. In all cases, the wing exhibited a gentle stall beginning at the tip. Tip stall is indicated by the increase in pitching moment (nose-up), which was due to the forward movement of the center of pressure as the lift from the tip section decreased. The presence of the ice shape did not dramatically change the stalling characteristics of the wing. Whereas the behavior of the lift curve after stall differed from the clean wing, a gentle tip stall still occurred, although the increase in pitching moment was not as large as in the clean case.

Because of the lack of a true maximum C_L, the stalling angle of attack (α_{stall}) is defined here as the angle of attack at which the pitching moment is minimum. Although this point may not coincide with the maximum lift coefficient, it is associated with an unstable break in pitching moment and a break in the drag curve. This increase in pitching moment is due to tip. The angles of attack and lift coefficients corresponding to the minimum pitching moment for the clean and iced wing are summarized in tables 3 and 4, respectively. Figure 6 shows that α_{stall} also marks a change in the lift curve slope, and at angles past α_{stall}, the drag coefficient increases rapidly. The decrease in the lift curve slope was due to a change in the aerodynamic performance of the outboard sections of the wing. The ice decreased the stalling angle by 2.65º for the lowest Reynolds number and 4.65º at the highest. In addition, $C_{L,Stall}$ was reduced by an average of 38.4%. The data in tables 3 and 4 also show a reduction in the influence of the Reynolds number for the iced wing. This is consistent with results for iced airfoils. The presence of the ice shape fixes the leading-edge separation point, resulting in reduced Reynolds number effects [1].

Table 3. α_{Stall} and $C_{L,Stall}$ for the clean wing (stall defined at $C_{M,min}$)

RE ($x10^5$)	α_{stall}	$C_{L,stall}$
3.0	8.60	0.70
6.0	9.65	0.78
7.8	10.2	0.82

Table 4. α_{Stall} and $C_{L,Stall}$ for the iced wing (stall defined at $C_{M,min}$)

RE ($x10^5$)	α_{stall}	$C_{L,stall}$
3.0	5.95	0.53
6.0	5.98	0.56
7.8	5.98	0.57

Figures 7–9 compare surface-pressure distributions of the clean and iced wing at the first four rows of pressure taps for different angles of attack and RE = $6x10^5$. Note that the three figures do not have the same scale for the *y*-axis. Figure 7 compares pressure distributions at $\alpha = 3.3°$. At this angle of attack, a suction peak can be seen at the leading edge for both a clean and iced wing. For the iced wing, the suction peak resulted from flow accelerating over the tip of the ice shape. At spanwise locations of $2y/b = 0.36$ and 0.55, the suction peak of the iced wing is broader than the clean wing because of a small region of separated flow. Figure 8 compares pressure distributions at $\alpha = 5.5°$. At this angle of attack, the suction peak of the iced wing has decreased relative to the clean wing peak and has broadened further as the region of separated flow has grown in the streamwise direction. Figure 9 shows that the clean and iced wing are no longer at the same angle of attack, but they are both beyond their respective stalling angles of attack. The two inboard rows of the clean wing still exhibit a significant suction peak, but the outboard two sections have a reduced and broadened peak. This indicates that the flow over the outboard section of the clean wing has separated, which is consistent with tip stall indicated by the pitching moment. For the iced wing, the suction peak was reduced and broadened at all spanwise locations, indicating a further increase in the size of the separated region.

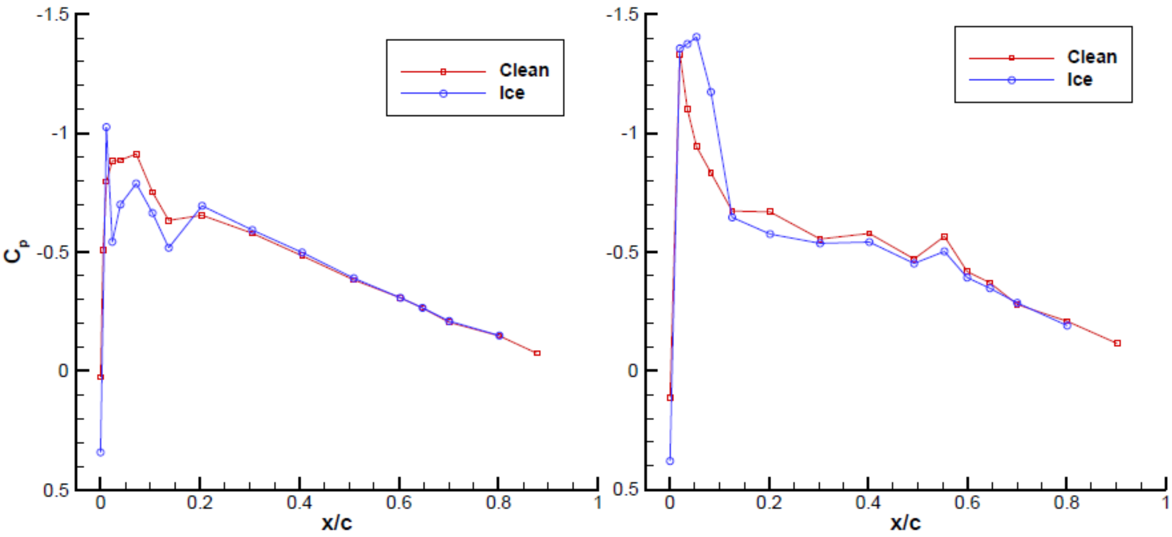

a) 2y/b = 0.11 b) 2y/b = 0.36

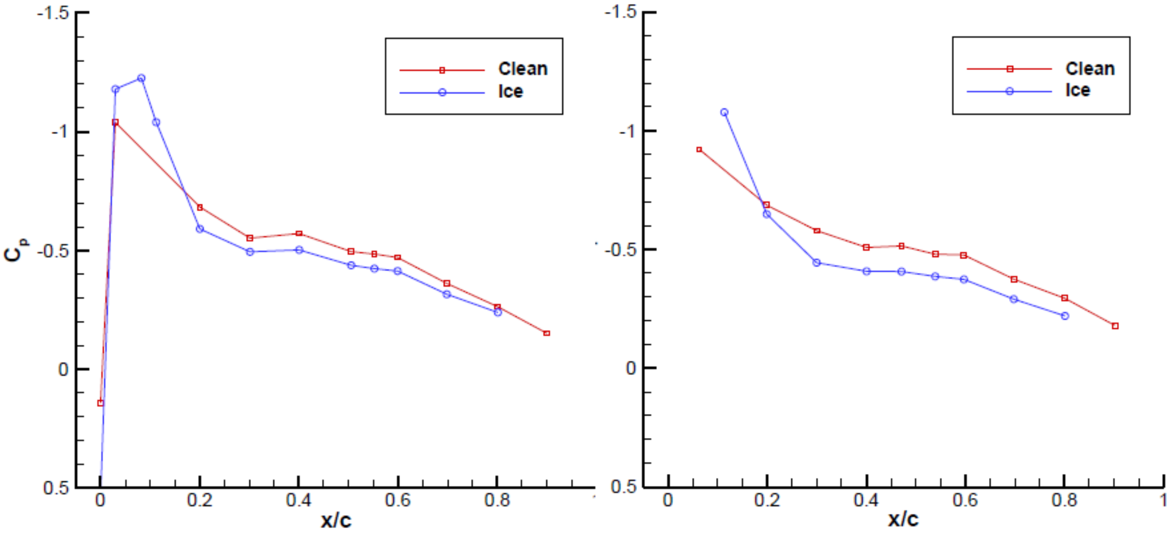

c) 2y/b = 0.55 d) 2y/b = 0.77

Figure 7. Comparison of clean and iced wing CP distributions for rows 1–4 (A = 3.3º, Re = 6X105)

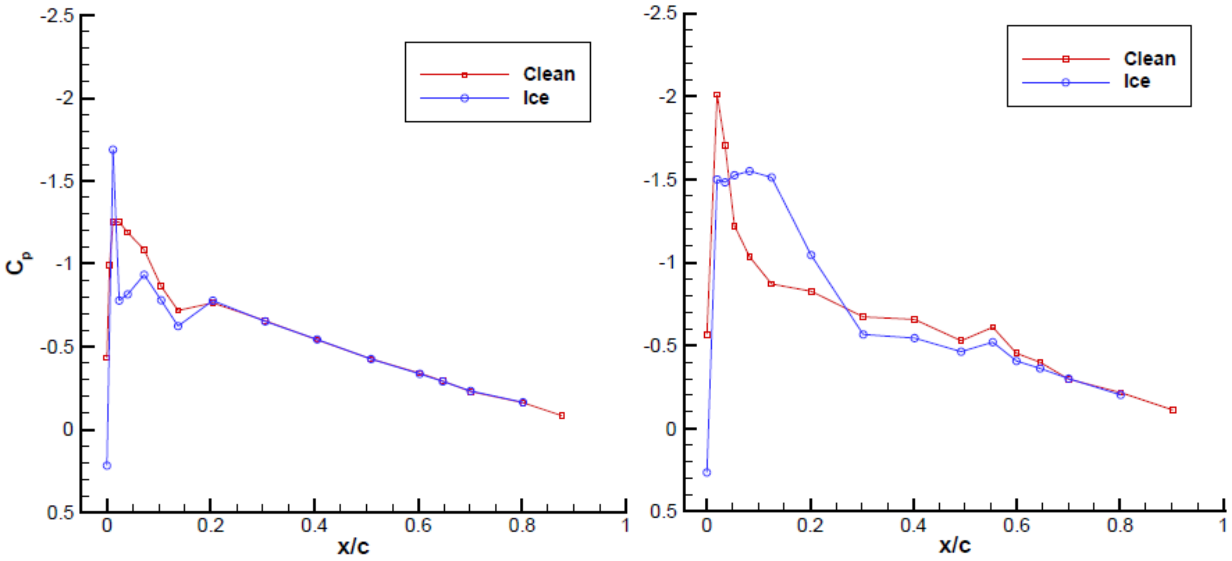

a) 2y/b = 0.11

b) 2y/b = 0.36

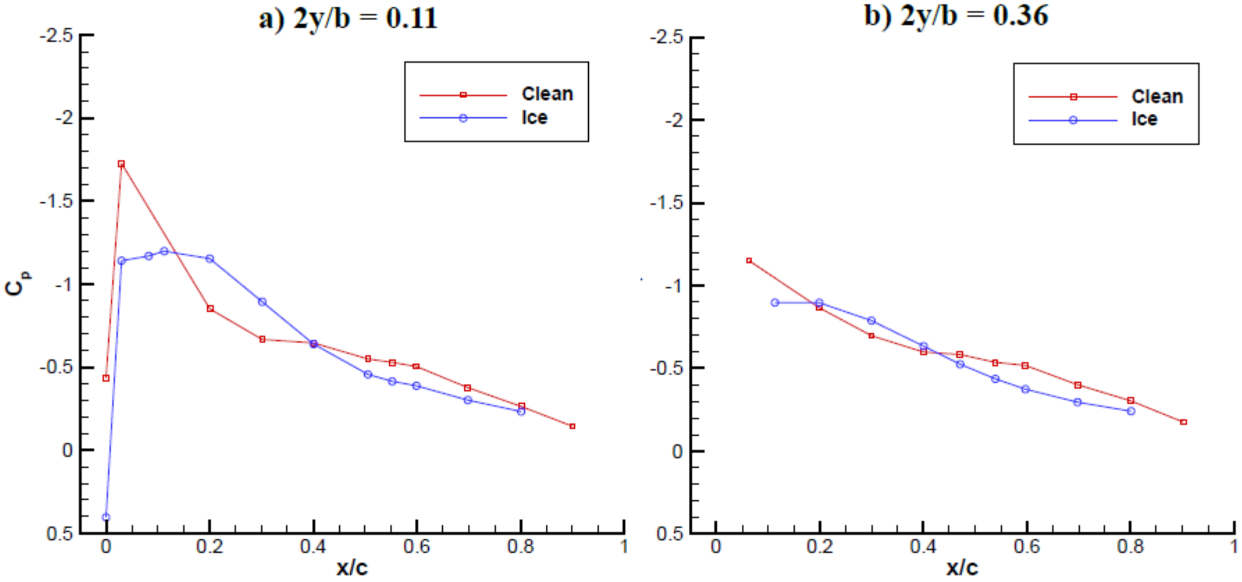

c) 2y/b = 0.55

d) 2y/b = 0.77

Figure 8. Comparison of clean and iced wing CP distributions for rows 1–4 (A = 5.5, Re = 6X105)

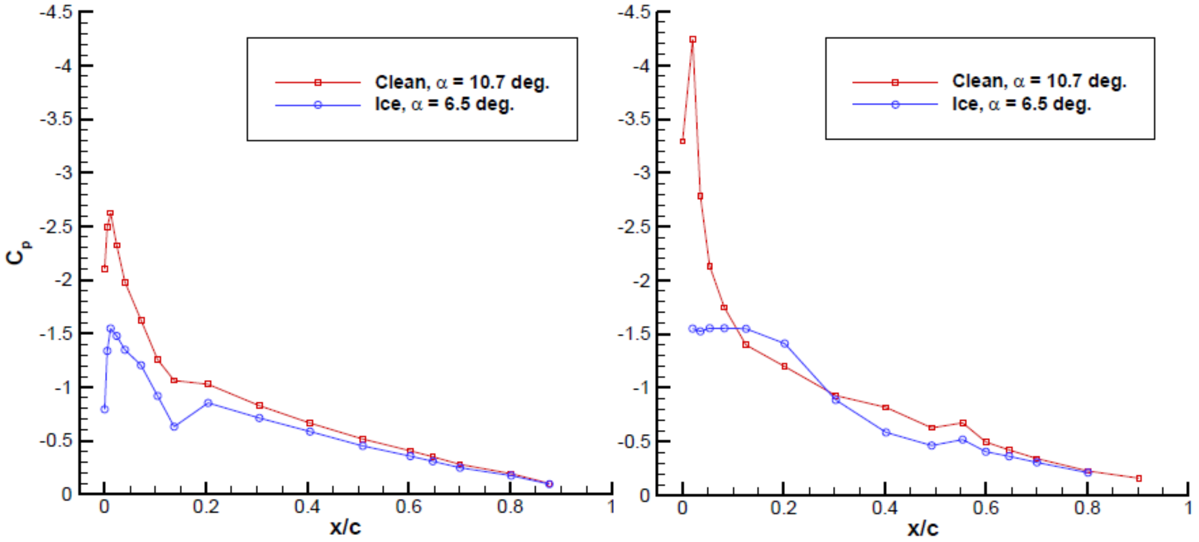

a) 2y/b = 0.11 b) 2y/b = 0.36

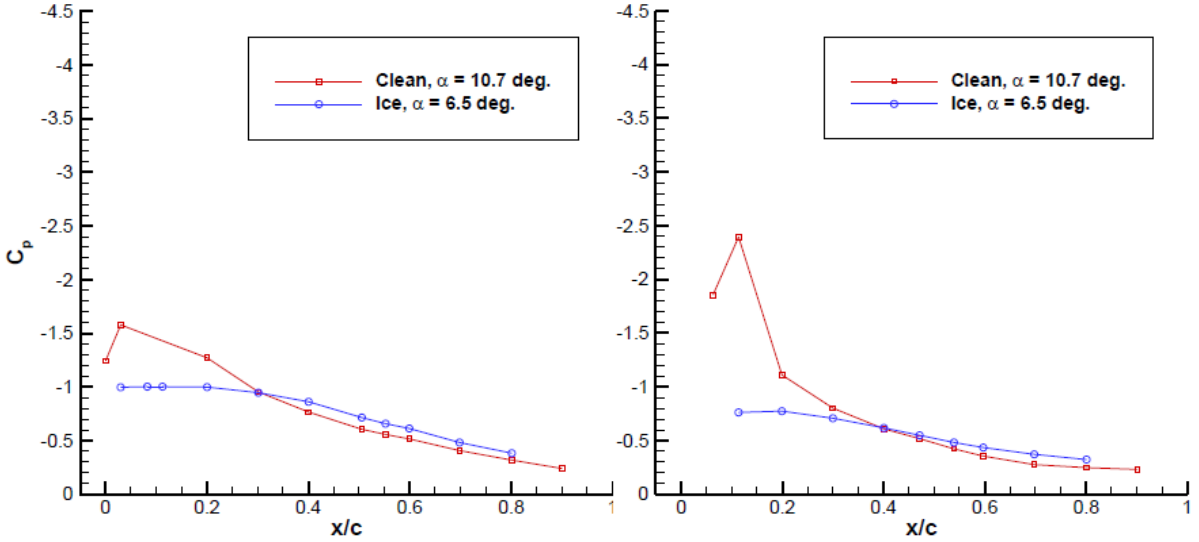

c) 2y/b = 0.55 d) 2y/b = 0.77

Figure 9. Comparison of clean- and iced-wing CP distributions for rows 1–4 (both wings beyond their respective α_{stall}, Re = 6X105)

5.4 SURFACE OIL FLOW VISUALIZATION

Surface oil flow visualization was also performed in addition to the force-balance and surface-pressure measurements. This method involves the application of a mixture of mineral oil and fluorescent dye on the surface of the model. The shear from the flow moves the oil along the surface. The pattern of oil can then be viewed with a UV lamp showing the major features of the flow near the surface. Figure 10 shows the surface oil flow for the clean wing for a range of angles of attack. The flow changes significantly as the angle of attack is increased. At α = 2.3º, along most of the span, a region of low shear or separated flow had developed near approximately 50% chord. A line of oil accumulation near the trailing edge of the outboard section of the wing indicated a region of separated flow over the aft section of the chord, followed by a reattachment line. A reattachment line divides flow moving in the upstream and downstream direction and forms when separated flow reattaches to the surface. The flow moving in the upstream direction is terminated by the oil-accumulation line, indicating secondary separation. The flow at α = 3.3º was similar, but in regions where the flow separation did occur, the reattachment line was further upstream, and flow was attached over a greater percentage of the chord. It should be noted that at these low angles of attack, there were several oil-accumulation lines near the leading edge, most notably for α = 3.3º. These lines were a result of separation due to the small steps and imperfections where the leading edge met the upper surface.

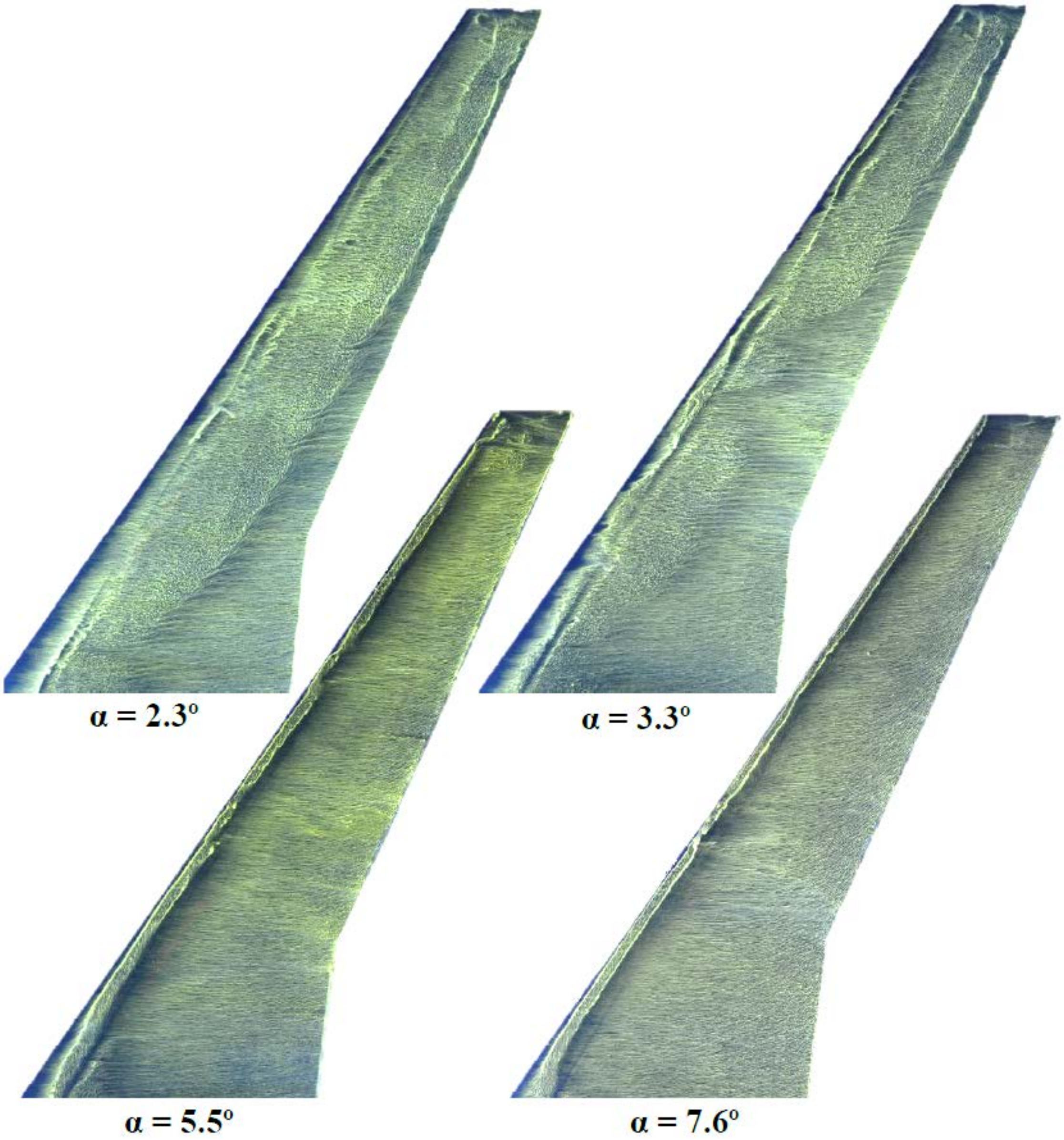
$\alpha = 2.3^\circ$

$\alpha = 3.3^\circ$

$\alpha = 5.5^\circ$

$\alpha = 7.6^\circ$

Figure 10. Oil flow images of the clean wing over a range of angles of attack

The oil flow for the clean wing shows that a very different flowfield occurred at α = 5.5º and α = 7.6º. At the higher angles, the flow separated from the upper surface near the leading edge because of the adverse pressure gradient. This separation was quickly followed by reattachment along the entire span. Figure 11 shows the important features of the separated flow near the leading edge for the clean wing at α = 5.5º. The first oil-accumulation line labeled "Primary Separation" indicates where the flow initially separated. The separated shear layer then rolled up to form a vortex, which reattached at the point marked "Reattachment." The actual reattachment line is difficult to see in this image because of the oil having been sheared away. The second oil-accumulation line marks the "Secondary Separation" of the boundary layer under the vortex flowing upstream. Comparing the images for α = 5.5º and α = 7.6º in figure 10 downstream of reattachment the oil flow shows increased spanwise flow for the higher angle of attack because of the increased spanwise pressure gradient.

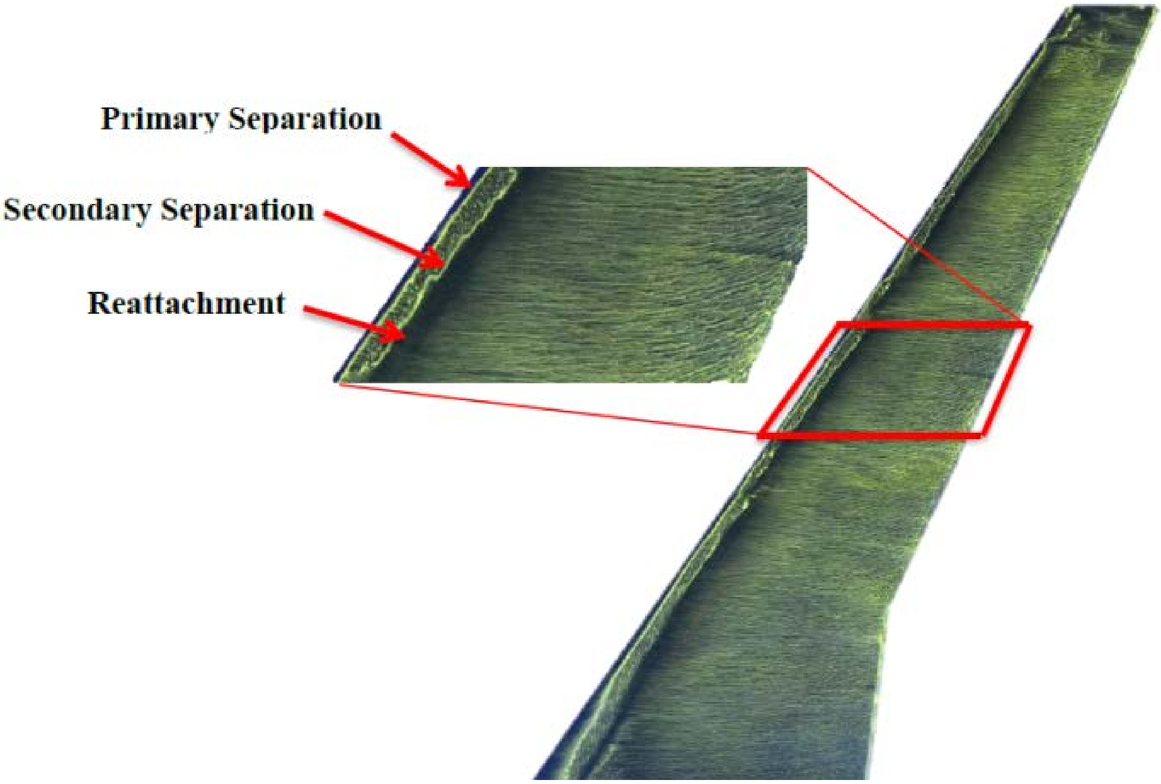

Figure 11. Features of leading-edge vortex (clean wing, A = 5.5º)

Figure 12 shows the oil-flow pattern on the stalled clean wing at α = 9.6º. The oil flow shows that leading-edge separation occurred along nearly the entire span. On the inboard stations, the flow quickly reattached and the primary-separation, reattachment, and secondary-separation lines are visible. At approximately 30% span, near the Yehudi break, the size of the separated region began to increase rapidly, and the flow failed to reattach on the outboard sections. The separated flow rolled up to form a leading-edge vortex due to the spanwise pressure gradient, and as the vortex grew it curved away from the leading edge in the downstream direction and was ultimately shed into the wake outboard of midspan.

Figure 12. Oil flow of the stalled clean wing (A = 9.6º)

Figure 13 shows the flowfield of the iced wing over a range of angles of attack. The flowfield of the iced wing was significantly different from the clean wing. For the iced wing, beginning at the lowest angle of attack shown, the flow initially separated at the tip of the ice shape and then rolled up and reattached to the surface, forming a leading-edge vortex along most of the span. The flow downstream of this vortex was fully attached. Unlike the clean wing, the general features of the iced-wing flowfield did not change significantly with angle of attack over this range.

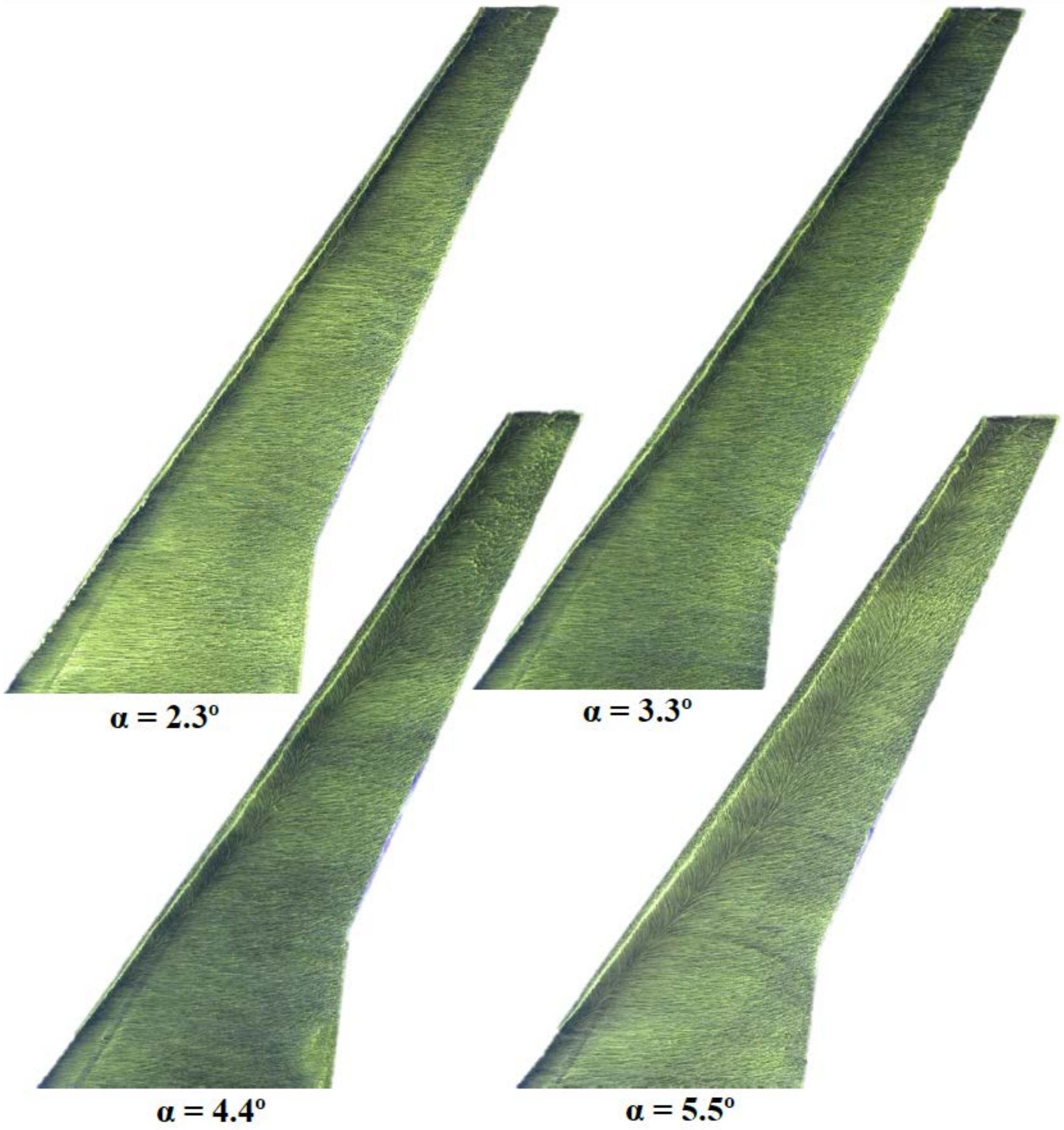

$\alpha = 2.3^{\circ}$ $\alpha = 3.3^{\circ}$

$\alpha = 4.4^{\circ}$ $\alpha = 5.5^{\circ}$

Figure 13. Oil-flow images of the iced wing over a range of angles of attack

Figure 14 shows the important features of the leading-edge vortex on the iced wing at $\alpha = 5.5^{\circ}$. The separated region of the iced wing contained the same features as the separated flowfield of the clean wing shown in figure 11. For the iced wing, primary separation was located at the tip of the ice shape, and compared to the clean wing, the reattachment line was significantly further downstream, indicating a larger leading-edge vortex. The 3D flow within this vortex is clearly visible. As the boundary layer flowed in the upstream direction from the reattachment line, it initially experienced a favorable pressure gradient, although it passed under the vortex core. After passing under the core, the boundary layer experienced an adverse pressure gradient, which forced it to separate at the secondary separation line.

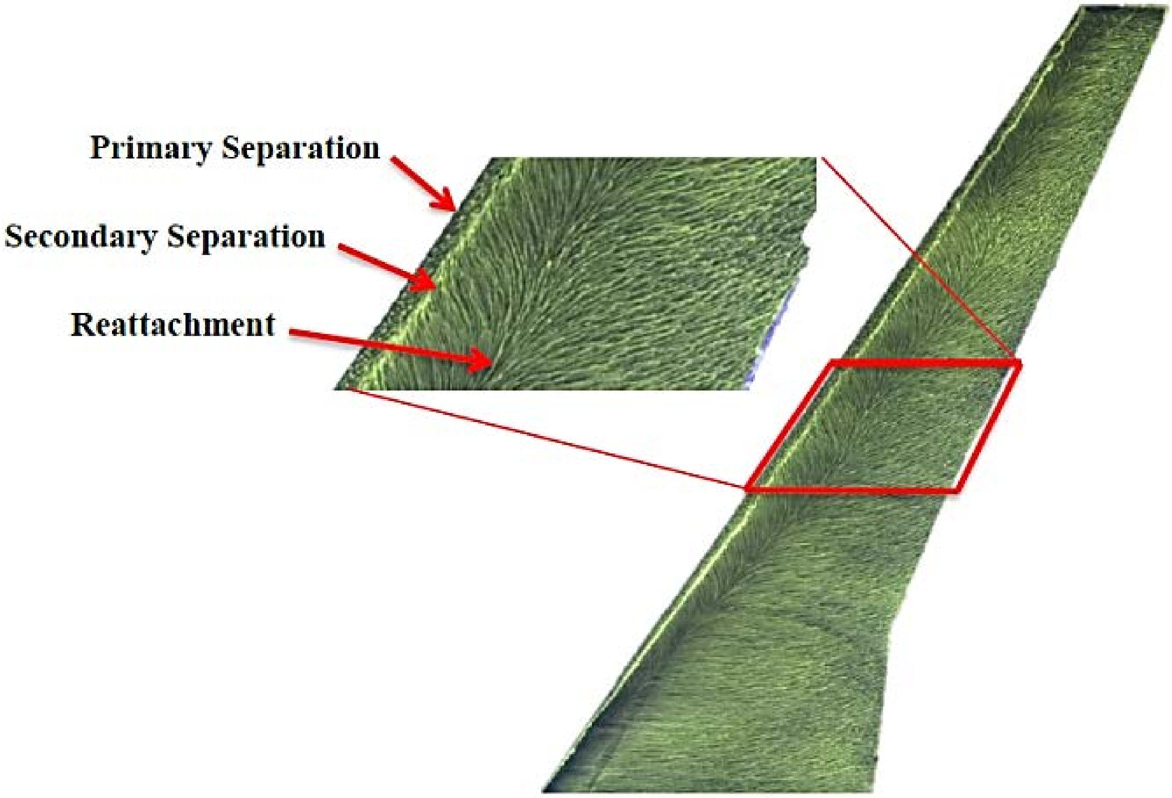

Figure 14. Features of leading-edge vortex (iced wing, A = 5.5º)

Figure 15 shows the oil-flow images of the iced wing from figure 13 with the reattachment lines highlighted. The figure shows that, as the angle of attack was increased, the start of the leading-edge vortex moved inboard toward the root; but, more importantly, the reattachment line moved downstream, indicating that the size of the leading-edge vortex increased with angle of attack. This is similar to the flowfield behind a horn ice accretion on an airfoil. For the 2D case, the flow separates from the tip of the horn and reattaches downstream, forming a recirculation region. As the angle of attack increases, the point of reattachment moves downstream and can grow as large as 40% or more of the chord before it fails to reattach and the airfoil stalls [1]. Whereas the leading-edge vortex of the ice- wing flowfield contained similarities to the recirculation region of the iced airfoil, there were important differences due to 3D effects. The oil flow clearly indicated spanwise flow within the boundary layer under the vortex, and the reattachment lines in figure 15 show that as the angle of attack was increased, significant spanwise variation in the vortex occurred. At the higher angles of attack, several kinks developed in the reattachment line. It is interesting to note that, in general, the size of the separated region relative to the local chord of the wing increases in the outboard direction. There were several 3D mechanisms, which likely influenced the size and shape of the leading-edge vortex, including the size of the ice shape relative to the local chord, the local angle of attack, the spanwise pressure gradient, shear-layer instabilities, and the state of the boundary layer under the vortex. Some or all of these mechanisms may have been responsible for the observed flowfield.

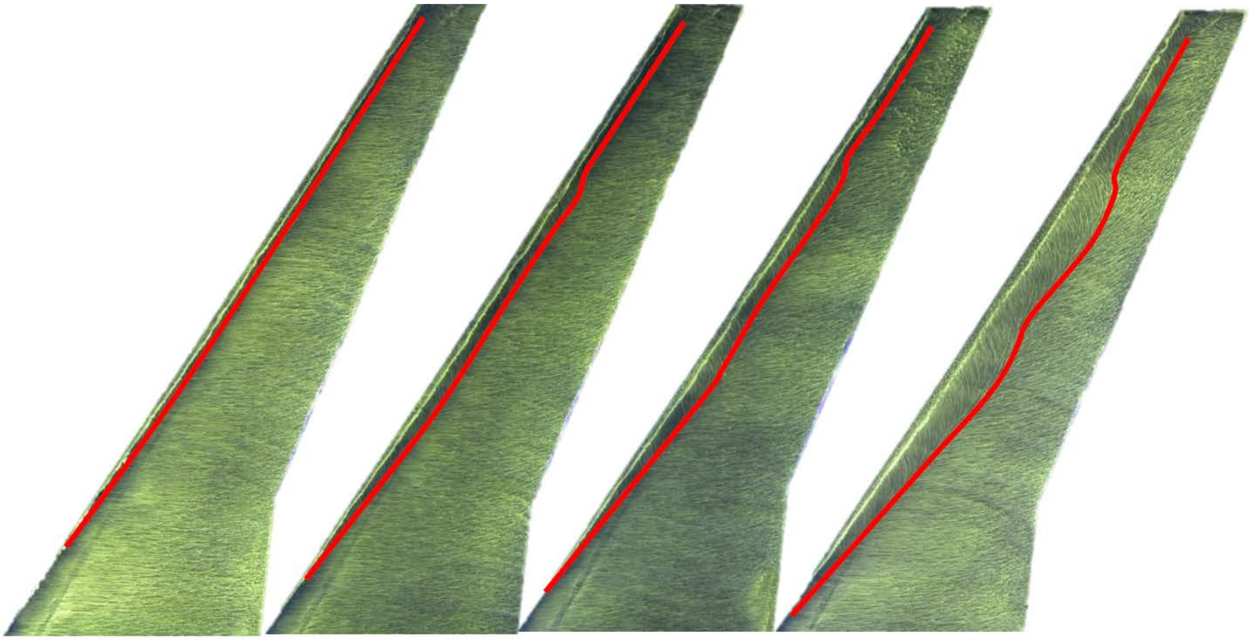

α = 2.3° α = 3.3° α = 4.4° α = 5.5°

Figure 15. Reattachment line of the separated flow on the iced wing for a range of angles

The oil flow of the stalled iced wing at α = 6.5º is shown in figure 16. Beginning near the root, the size of the leading-edge vortex grew gradually, and the flow reattached behind the vortex similar to the lower angles of attack. The flow failed to reattach near approximately midspan, and the flow on the surface of the outboard sections was in the upstream direction. Compared to the clean wing, the leading-edge vortex of the iced wing began closer to the root and grew at a slower rate. The vortex of the iced wing was also shed into the wake just outboard of midspan.

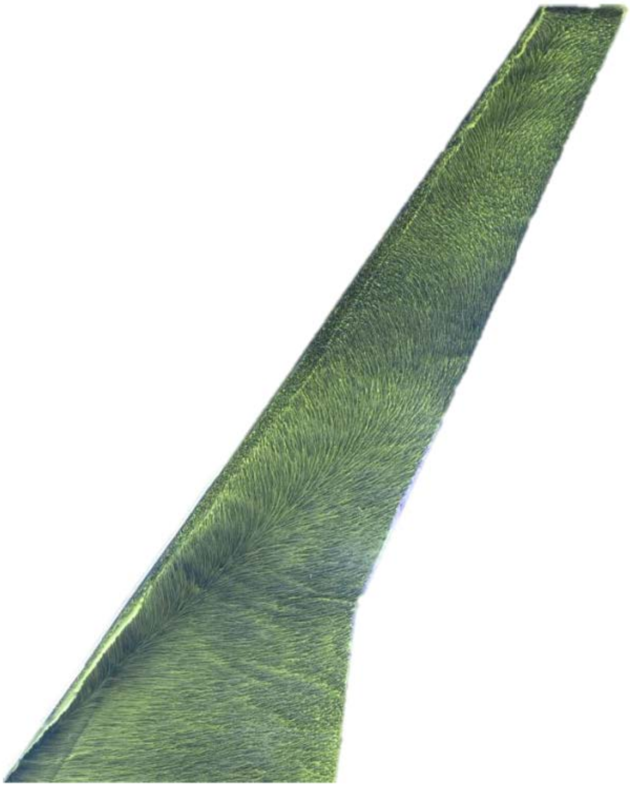

Figure 16. Oil flow of the stalled iced wing (A = 6.5º)

5.5 PRESSURE-SENSITIVE PAINT

One of the goals of the research at UIUC was to investigate and develop advanced experimental techniques with the potential to provide valuable information regarding the effects of ice on swept wings. One such technique investigated at UIUC was pressure-sensitive paint (PSP). When luminescing particles in PSP are excited using a high-energy source, such as a lamp or laser, the particles absorb the radiative energy from the photon so that the electrons in the paint transition to higher energy levels [22]. The electrons can return to their ground state by emitting a photon at a longer wavelength than that of the excitation source. The electrons can also return to their ground state through the interaction of fluorescent molecules and oxygen without the emission of a photon. As a result, the local intensity emitted by the paint depends on the local concentration of oxygen, which is proportional to the local pressure. By imaging the surface with a charge-coupled device (CCD) camera and calibrating the measured intensity using surface-pressure taps, it is possible to obtain a nearly continuous pressure distribution over the surface. When investigating the aerodynamics of iced airfoils, pressure taps are sufficient because of the 2D nature of the flow. In the case of a swept wing with a 3D artificial ice shape, the surface-pressure distribution can be highly 3D, and the high resolution of PSP is potentially valuable.

The experimental setup for PSP is relatively straightforward requiring a painted surface, a lamp, and a CCD camera, as shown in figure 17. Examples of the results obtained from PSP are shown in figure 18 for the iced wing at several angles of attack and RE = 7.8×10^5. The continuous pressure distribution clearly shows that the leading-edge vortex is characterized by a region of low pressure.

The low pressure is due to the high-rotational velocities within the vortex. The lowest pressures are seen inboard near the leading edge where the vortex forms. The vortex grows in diameter along the span toward the tip and, as a result, the rotational velocities decrease, resulting in reduced suction.

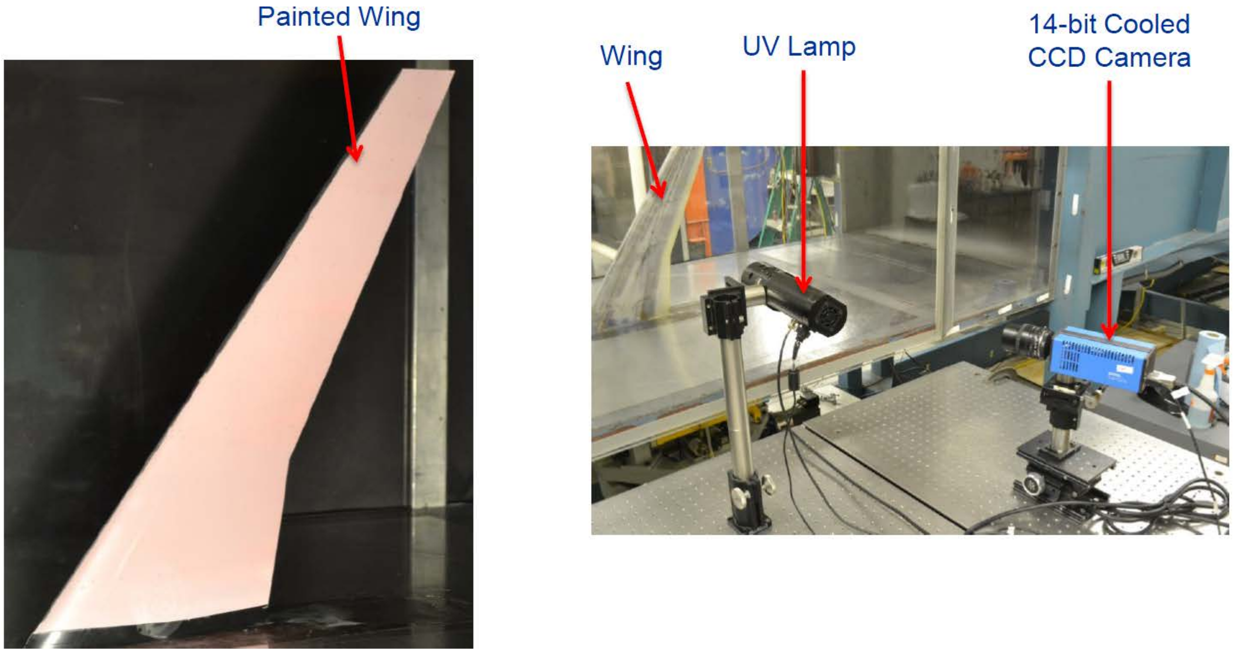

Figure 17. The PSP experimental setup at UIUC

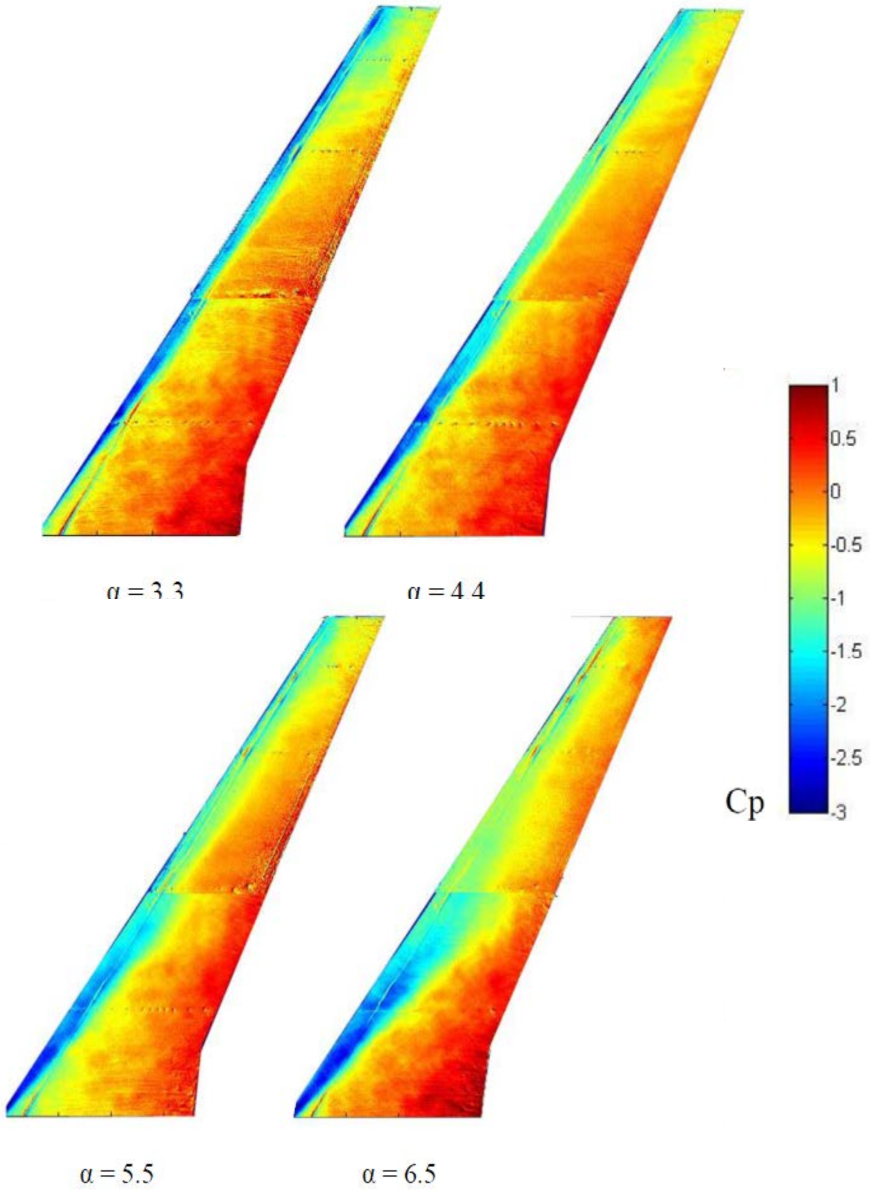

Figure 18. The PSP results for the iced wing at several angles of attack (Re = 7.8X105)

There is a discontinuity in the C_p distributions around midspan. Because of the wing size, it was necessary to acquire PSP images of the inboard and outboard sections of the wing separately, and it was necessary to move the camera and lamp to switch sections of the wing. As a result, the inboard and outboard images were not acquired with the same viewing angle and level of illumination. This can be fixed by mapping the 2D images onto the 3D surface of the wing using a method known as image resection. This technique was not used in this research.

However, the most significant challenges related to PSP are the effects of temperature and model motion. The intensity of light emitted by PSP is also dependent on temperature, which is a significant source of error in PSP experiments. Model motion can create a problem in two ways. First, if the model is undergoing unsteady motion, the image will be blurred. Second, PSP requires a reference image to be acquired with the wind tunnel off. The final PSP result requires a ratio of the wind-on image and the wind-off image. The loads on the model during testing cause the model to deflect. This will affect the ratio of the two images because the model has moved relative to the wind-off case. This error can be minimized with the use of image-processing techniques. Currently, there are no plans to pursue PSP further or to use the technique in future aerodynamic testing. Whereas PSP is potentially a valuable tool, it has been determined that other measurements will be more valuable within the constrained aerodynamic wind-tunnel schedules.

5.6 WAKE SURVEY

Another experimental technique investigated and developed at UIUC for the iced swept-wing study was the five-hole probe (5HP) wake survey. A 5HP is a pressure probe capable of measuring total and static pressure and the 3D velocity vector at a point in space. Wake surveys are typically used when testing 2D airfoils to obtain an accurate sectional drag coefficient. A 2D wake survey requires measurements of total pressure in the wake of the body. The drag can be calculated through a control volume analysis. In three dimensions, the wake survey technique is more complex, but can provide more information. By measuring the total and static pressure and all three components of velocity in the wake, it is possible to calculate the lift and drag of the body and decompose the drag into profile and induced drag [23]. In addition, the spanwise distribution of lift and drag can be determined. This information cannot be obtained easily with other methods. A force balance provides the total lift and drag but no information regarding the spanwise distributions of the forces. Surface-pressure measurements can be used to obtain spanwise load distributions but require very high spatial resolution. Profile drag and induced drag can be estimated based on the relationship between the lift and drag coefficients measured by the force balance, but this requires relying on theory that may not be valid for a wing with leading-edge ice.

A series of experiments was carried out at UIUC to obtain 5HP measurements in the wake of the clean and iced model as a way to fully develop this method for the low-to-medium Reynolds number (7x10 testing at WSU) testing later in the program. The probe used in this study was an Aeroprobe Corporation model PS5-C318-152 5HP. The probe tip was conical with a base diameter of 0.125 in. The 5HP was traversed horizontally and vertically throughout a downstream plane in the wake to make measurements in the wake of the swept-wing model. The measurement plane was located 20.25 in. downstream of the trailing edge of the model tip, $2x/b = 0.804$. In the spanwise direction, the survey extended from $2y/b = 0.156$ to $2y/b = 1.101$, and in the normal direction from $2z/b = -0.207$ to $2z/b = 0.2$. This survey area captured the entire wake except for the portion of the span inboard of $2y/b = 0.156$. This region was not measured because of the influence of the floor boundary layer. A variable step size was used depending on where the probe was located relative to the swept-wing wake. Table 5 summarizes the various step sizes for both the vertical and horizontal axes for the various wake-survey regions. Information regarding the calibration of the 5HP, the data-reduction process, and the wake survey equations can be found in Diebold [20] and Diebold and Bragg [24, 25].

Table 5. Wake survey regions and step size

	Vertical Step Size		Horizontal Step Size	
Region	$0.15 \leq 2y/b < 0.9$	$2y/b \geq 0.9$	$\lvert 0.1 \rvert < 2z/b$	$-0.1 \leq 2z/b \leq 0.1$
Step size (2/b)	0.0198	0.0099	0.0149	0.0099
Step size (in.)	0.5	0.25	0.375	0.25

Figure 19 compares the total lift (figure 19(a)) and drag (figure 19(b)) measured by the force balance and wake survey for the clean and iced wing at RE = 6x10^5. Comparing the force-balance measurements and the wake survey results shows that the wake survey method was able to accurately determine the lift and drag. The average error, relative to the balance, in the lift calculated from the wake data was 3.05% and 2.3% for the clean and iced wing, respectively. For the drag, the average error was 14.6% and 13.3% for the clean and iced wing, respectively. Whereas the error in the drag was relatively large, figure 19(b) shows that the drag curve determined from the wake survey follows the curve from the force-balance measurements very well, but the wake survey consistently underpredicted the drag. A possible explanation is that the inboard 10% of the wake was not surveyed and, therefore, the drag contribution from this region would not have been captured. Corrections to the drag to account for this unmeasured wake region would have significantly reduced the overall error in drag measurement. This correction will be developed for the low-to-medium Reynolds number testing later in the program.

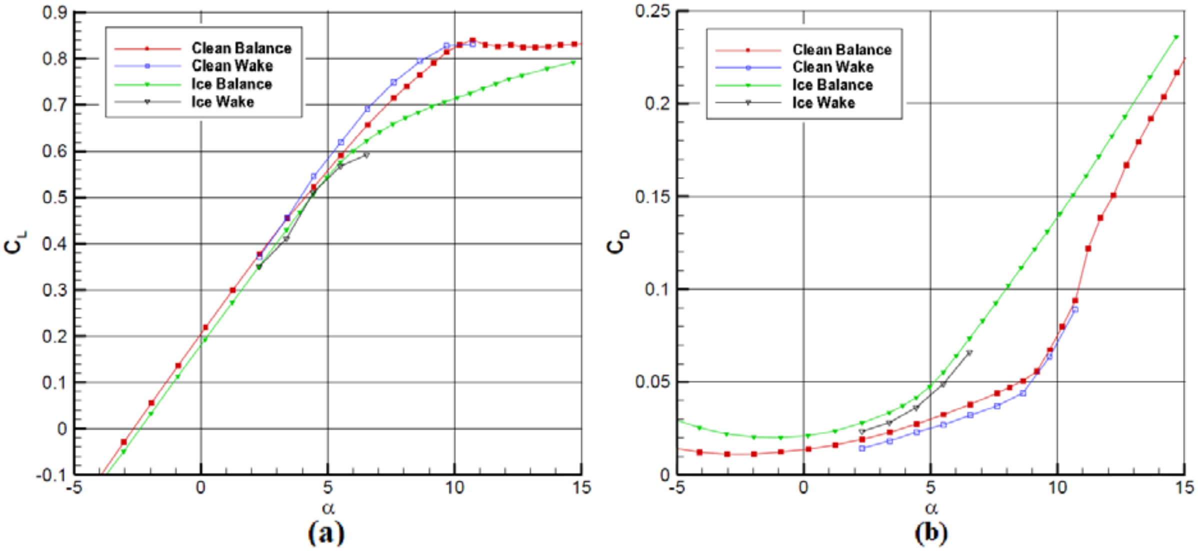

Figure 19. Comparison of lift (a) and drag (b) from the balance and wake (Re = 6X105)

Figure 20 shows the lift coefficient versus the decomposed profile and induced drag components for the clean and iced wing. The lift coefficient and drag coefficients were determined from wake survey data. The results show that, for a given C_L, the profile drag of the iced wing was significantly higher than for the clean wing. Over the range of C_L’s shown, the ice shape more than doubled the profile drag. This was expected given the large region of separated flow behind the ice shape seen in the oil-flow visualization. Figure 20 shows that as C_L was increased, the profile drag of the iced wing increased much faster than for the clean wing. This rapid increase in profile drag was due to the increasing size of the leading-edge vortex on the iced wing, as seen in figure 15. The induced drag was not significantly influenced by the presence of the ice shape. Figure 20 shows that the curves of C_L versus C_{Di} of the clean and iced wing almost exactly coincided for $C_L < 0.55$. As a result, for a given CL at an angle of attack below iced wing stall, the increase in drag due to the ice shape was nearly entirely due to a rise in the profile drag. Figure 20 also shows that the preponderance of the drag rise at stall for the clean and iced wing was due to a rise in the profile drag. These results show that the primary effect of the ice on the drag was to increase the axial momentum loss, a result primarily due to profile drag, as opposed to changing the amount of streamwise vorticity shed into the wake resulting from induced drag.

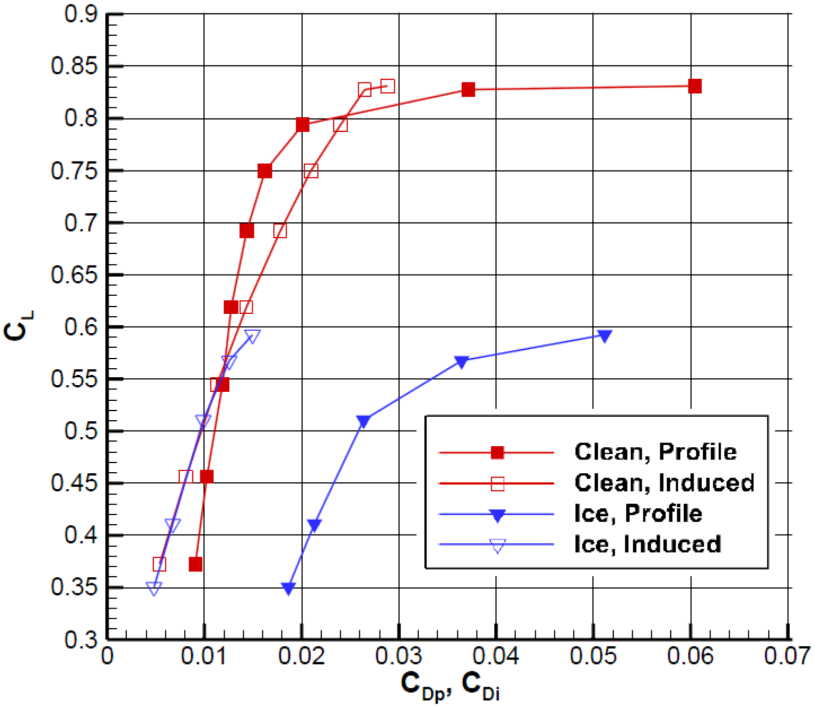

Figure 20. Components of drag for clean and iced wing (Re = 6X105)

Figure 21 shows the spanwise distributions of the lift coefficient and the total drag, profile drag, and induced drag coefficients for the clean and iced wing at α = 4.4º. Note that, because wake surveys were performed only at a few angles of attack, it was not possible to compare lift and drag distributions of the clean and iced wings for the same C_L. At α = 4.4º, total C_L and C_D of the clean wing measured by the force balance were 0.522 and 0.027, respectively. For the iced wing at α = 4.4º, total C_L and C_D were 0.5070 and 0.042, respectively. Over nearly the entire span, the local lift coefficient was decreased (see figure 21(a)) and the drag coefficient was increased (see figure 21(b)) by the presence of the ice shape. It can also be seen that the largest differences in the local lift and drag coefficients occurred outboard of approximately midspan. This was a consistent trend seen for all angles of attack: the local aerodynamic penalties were greater on the outboard sections of the wing when the ice was present. This was also seen in the oil-flow images (see figure 15), in which the size of the recirculation region occupied a larger percentage of the chord on the outboard sections of the wing. Figure 5 showed that the size of the ice shape relative to the local chord was much larger for the outboard sections of the wing, and this likely plays an important role in the ice shape having a larger effect near the tip.

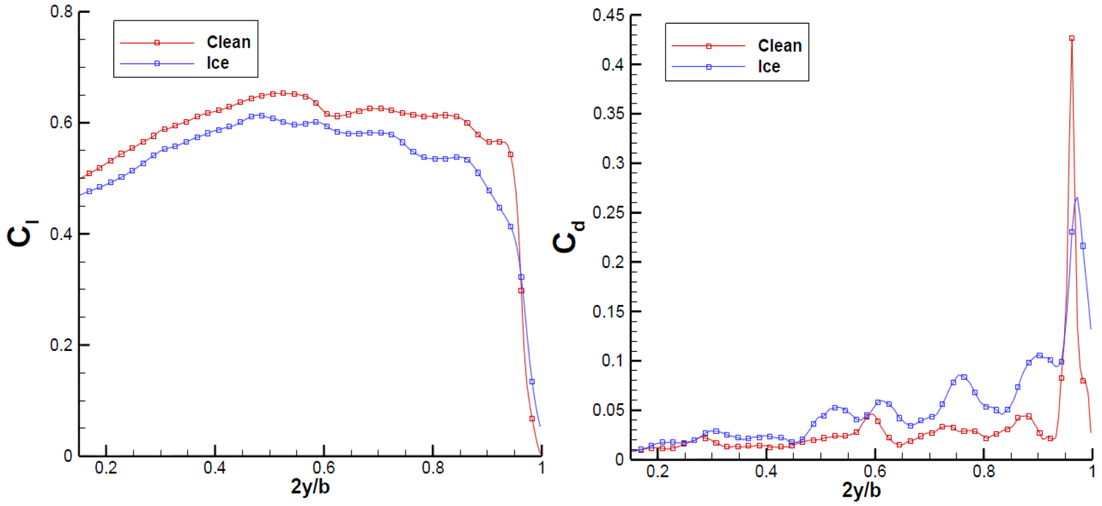

a) Lift Coefficient b) Drag Coefficient

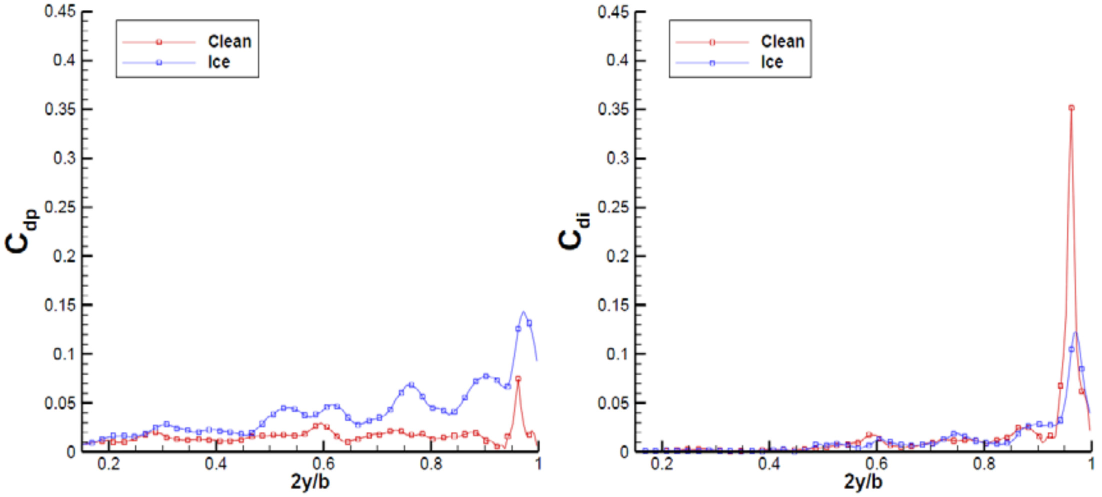

c) Profile Drag Coefficient d) Induced Drag Coefficient

Figure 21. Spanwise distributions of the (a) lift coefficient, (b) drag coefficient, (c) profile drag coefficient, and (d) induced-drag coefficient for the clean and iced wing (A = 4.4º, Re = 6X105)

The distributions of total, profile, and induced drag (see figures 21(b), (c), and (d)) show several local peaks along the span. These peaks were especially prominent for the iced wing. Figure 22 shows how the peaks in the profile drag coefficient of the iced wing at α = 4.4º corresponded to regions of concentrated axial velocity deficit in the wake. The contours represent streamwise velocity, and the vectors represent the cross-stream velocity. Although not shown here, the peaks in induced drag corresponded to regions of concentrated axial vorticity. The peaks in profile and induced drag occurred at the same location. In addition, figure 21(a) shows that at these same spanwise locations there is a decrease in the local lift coefficient. This indicates a change in the local circulation occurred, explaining the concentrated regions of shed vorticity. It is not surprising that peaks in the drag distributions corresponded to features in the wake because the distributions were determined from wake data, but these figures indicate that processes on the surface of the wing are causing vortex shedding and a loss of axial momentum.

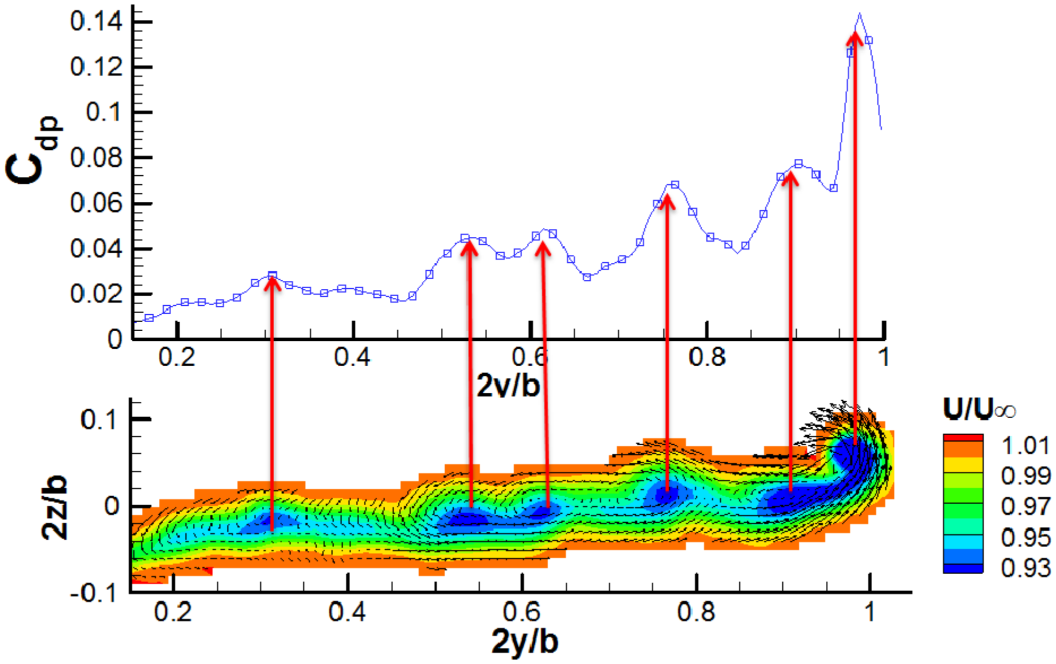

Figure 22. Correlation between regions of concentrated axial velocity deficit and local peaks in profile drag for the iced wing (A = 4.4º, Re = 6X105)

Figure 23 shows an attempt to relate features seen in the oil flow to features in the wake that correspond to peaks in the local drag coefficients of the iced wing at α = 4.4º. It can be seen that several concentrations of low axial velocity in the wake corresponded to local maxima in the size of the leading-edge vortex. This was observed for all angles of attack for the iced wing, as seen in Diebold [20]. Although it is unknown exactly why the size of the leading-edge vortex changed at these locations, it was clear that this had an effect on the local aerodynamic performance. When a local maxima in the leading-edge vortex was encountered, the local aerodynamics of this section were affected more than the neighboring sections because of the larger percentage of the chord being affected by the separated flow. This resulted in a local rise in the pressure drag, which is seen as the concentration in low axial velocity in the wake and a peak in profile drag. In addition, because of the larger separated region, the lift at these sections decreased slightly, resulting in vorticity being shed into the wake and the development of a peak in induced drag. One possible contributor to the local maxima in drag could be imperfections in the model. The stereolithography (SLA) skin of the model was affected by warping in the area of the removable leading edge and the upper surface of the wing. Although it is unfortunate that the model was slightly deformed, the fact that the wake-survey technique may be able to capture these features is promising. It indicates that the technique is sensitive to small changes in the geometry of the wing, which could be very valuable when studying highly 3D ice shapes.

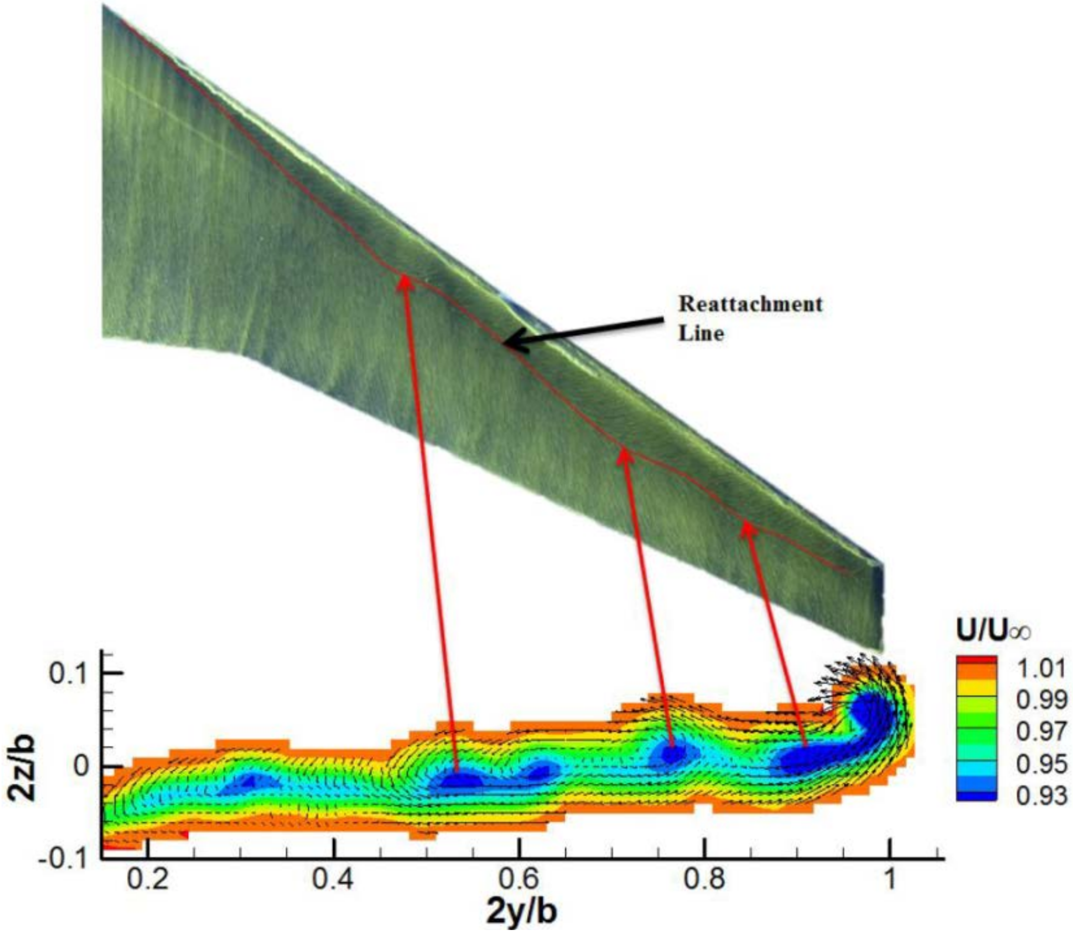

Figure 23. Correlation between features in the wake and the surface oil flow for the iced wing (A = 4.4º, Re = 6X105)

The wake survey results were also used to investigate the effects of stall on the clean and iced wing. Figures 24(a) and 24(c) compare the spanwise distributions of the clean wing lift and drag for an angle of attack just prior to stall (α = 8.6º) and just after stall (α = 10.7º); figures 24(b) and 24(d) compare the distributions of lift and drag for the iced wing just prior to stall (α = 5.5º) and just after stall (α = 6.5º). Note the difference in scales for the clean-wing figures and iced-wing figures. A direct comparison is not as useful because the stalling angles of attack are sufficiently different between the clean and iced cases.

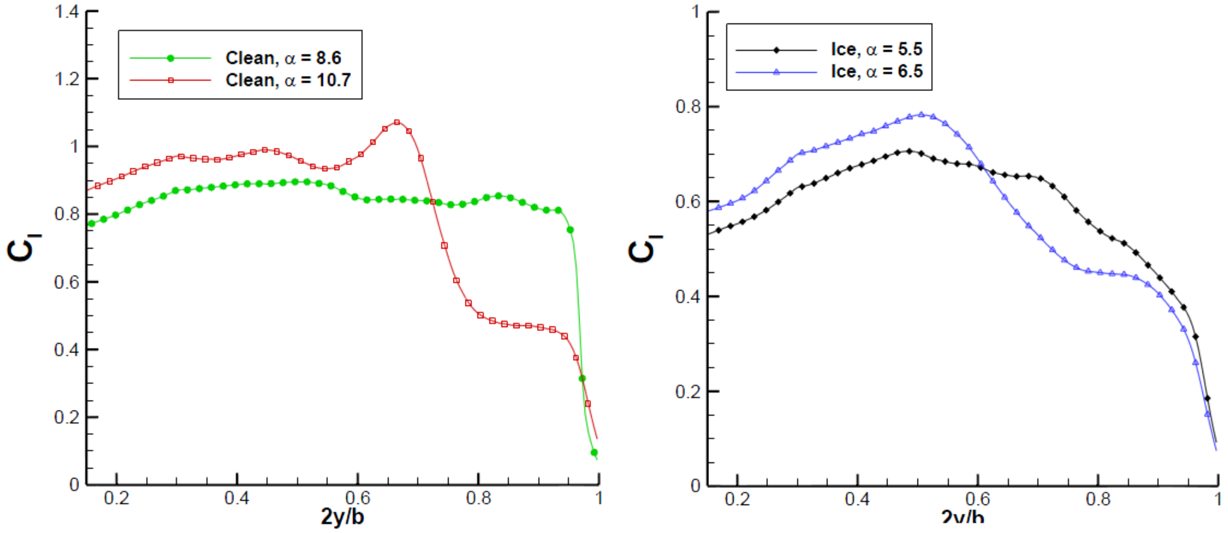

a) Clean Lift Coefficient

b) Ice Lift Coefficient

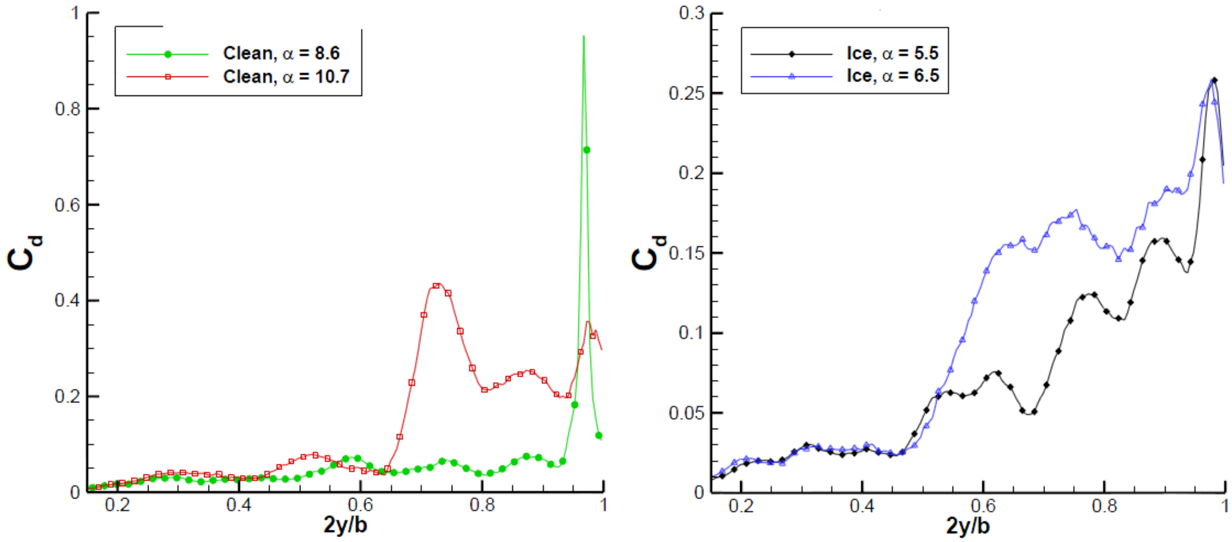

c) Clean Drag Coefficient

d) Ice Drag Coefficient

Figure 24. Comparison of pre- and post-stall spanwise distributions of the (a) clean wing-lift coefficient, (b) ice wing-lift coefficient, (c) clean wing-drag coefficient, and (d) ice wing-drag coefficient (Re = 6X105)

The oil flow images (figures 12 and 16) show that stall of the clean and iced wing occurred when the flow separated from the leading edge and failed to reattach along the chord of the wing. The separated flow rolled up to form a leading-edge vortex, which was shed into the wake at approximately 2y/b = 0.6. The flow inboard of the vortex remained attached, whereas outboard the flow on the surface was fully reversed. The effects on the lift distribution can be seen in figures 24(a) and 24(b). The lift on the inboard sections continued to increase through stall for both the clean and iced wing, and the lift on the outboard sections decreased significantly because of the separated flow. These results explain the behavior of the lift curve after stall, as seen in the force-balance measurements in figure 6. The lift did not decrease as a result of stall for both the clean and iced wing. For the clean wing, the lift was nearly constant as the angle of attack continued to increase, whereas, for the iced wing, the lift continued to increase, but the slope of the curve had decreased. The wake survey results show that the inboard sections of the wing were able to compensate for the loss of lift produced by the outboard sections and prevented the lift from decreasing. This also confirms the observations made regarding the pitching moment of the wing. As the lift on the outboard sections decreases, the center of pressure of the swept wing moves forward, resulting in a nose-up change pitching moment.

5.7 FAST REPONSE 5HP

The wake-survey technique used at UIUC is derived from the standard 5HP wake survey method [23]. A potential serious drawback of the standard 5HP wake survey is the influence of turbulence in the wake. Turbulence can influence the wake survey in two ways. First, when deriving the wake survey equations for drag, it is assumed that the turbulence is negligible. It has been shown that neglecting the turbulent stresses in the 2D wake survey of a cylinder and stalled airfoil with an ice shape can result in underpredicting the drag by 5%–20% [26]. In addition, turbulence is known to bias the measurement of total pressure by standard pressure probes, resulting in error in the measured velocities. Work is currently underway at UIUC to improve the wake-survey technique with the use of a fast response 5HP (FR5HP). The FR5HP is a 5HP with high-frequency response pressure transducers embedded near the tip of the probe. The probe is capable of time-resolved measurements of the total pressure, static pressure, and the full velocity vector. These measurements can be used to determine the level of turbulence, which can then be used to correct the pressure measurements and keep the turbulent stresses in the wake-survey equation. This will allow for a more accurate determination of the drag.

5.8 SPLITTER PLATE EXPERIMENTS

The wind-tunnel experiments discussed above, and the future experiments planned for this program, use a semispan swept-wing model rather than a full-span wing. The semispan technique has several important advantages over a model of a complete aircraft. Semispan models can typically achieve double the Reynolds number of a similar full-span model because of the increased size. Additional benefits of the large model size include improved model strength, higher geometric fidelity, and more room for instrumentation. The semispan model can also typically be constructed for less cost if complex features, such as high-lift systems or flow-through nacelles, are required [27]. The primary drawbacks to the semispan model include increased wind-tunnel wall effects because of the large model size and, more importantly, the aerodynamic influence of the specific sidewall or floor-mounting method. Unlike a full-span model, a semispan wing does not require any sting or support strut, and there are several ways in which a semispan wing is typically mounted in a wind tunnel. The most straightforward method is to simply mount the wing directly to the tunnel floor. A semispan model is typically one side of a symmetric geometry, so ideally the tunnel floor would act as a reflection plane boundary condition. Unfortunately, there are several ways in which the tunnel-floor boundary layer can influence the aerodynamics of the semispan model and alter the simple inviscid reflection plane boundary condition. First, the loading near the root of the semispan wing is reduced because of the low dynamic pressure in the tunnel-floor boundary layer. Second, the tunnel-floor boundary layer can separate near the wing's leading edge, resulting in the formation of a horseshoe vortex system. Finally, the adverse pressure gradient along the surface of the wing can cause the tunnel-floor boundary layer to separate anywhere along the aft section pressure recovery regions of the wing root. These modifications to the flowfield resulting from the tunnel-floor boundary layer can lead to a reduction in the lift curve slope, increased zero-lift incidence, and increased drag on the semispan wing compared to the full-span [28–30].

There are several common methods to minimize the influence on the tunnel boundary layer, including the use of a half-fuselage and standoff, boundary-layer suction, and a splitter plate. The use of a half-fuselage is common and involves splitting the aircraft exactly at the plane of symmetry. A potential disadvantage of this method is the high cost of constructing the half fuselage, and if the fuselage is properly scaled it may be necessary to reduce the scale factor of the entire model geometry, resulting in a smaller wing. In addition, the use of the half-fuselage does not eliminate the influence of the floor boundary layer. The half-fuselage must be raised out of the boundary layer through the use of a standoff, also known as a spacer or peniche. There have been numerous experimental and numerical studies investigating the influence of the standoff height and shape on the performance and flowfield of a semispan wing [29, 31]. The performance of the wing can be very sensitive to the standoff geometry, especially at high angles of attack near stall. Boundary layer suction has also been used in several studies [31, 32]. Studies using suction with the wing mounted directly to the tunnel floor have shown that suction only applied ahead of the model does not have a significant impact on the aerodynamics of the semispan wing, and it is necessary to apply suction around the entire root of the wing. Suction also requires a complex pumping system beneath the tunnel floor, and it is difficult to know the correct amount of suction to apply. In addition, the amount of suction required may change with freestream conditions, model configuration, and angle of attack.

Both the half-fuselage and suction techniques have received a fair amount of attention in the literature. There is comparatively very little regarding the use of a splitter plate. A splitter plate is a flat surface that is raised above the floor of the tunnel, typically just above the floor boundary layer. Mounting the semispan model to the splitter plate is similar to mounting it directly to the tunnel floor. A boundary layer still forms on the surface of the splitter plate and can still negatively interact with the wing. Ideally, the advantage of a splitter plate is that the boundary layer on the plate will be significantly thinner than the boundary layer on the floor, which will reduce the negative interactions with the flow over the model. For a splitter plate to act as an ideal reflection plane, the boundary layer must be thin with no pressure gradient at the model mounting location. This is not easily achieved because of the way in which the splitter plate can alter the flow in the tunnel. Giguere and Selig [33] discuss the use of splitter plates for 2D airfoil testing and explain several ways in which the splitter plate can affect the flow. Flow must go under the splitter plate, and this flow can be deflected because of the presence of the plate supporting structure and the boundary layers under the plate. There are two boundary layers in the area between the splitter plate and the floor – one on the tunnel floor and another on the underside of the plate. These two boundary layers grow and further restrict the flow. The blockage effects caused by the presence of the plate and the additional boundary layer force the flow to deflect and cause the leading edge of the plate to be at an angle of attack relative to the local flow, even though the plate is parallel to the freestream. This effective angle of attack can lead to leading-edge separation on the plate, which results in a large boundary layer and a pressure gradient on the plate.

For the swept-wing icing program, it was determined that the splitter plate was the most appropriate choice for mounting the semispan model in the larger wind-tunnel facilities. This decision was made based on the simplicity and low cost of constructing a splitter plate. An extensive literature review did not find any guidelines for how to properly design a splitter plate. As a result, a series of wind-tunnel tests were carried out at UIUC to better understand how the geometry of the splitter plate influences the flow over the plate. Two different splitter plate experiments were performed. First, the Variable Geometry Splitter Plate Experiment investigated the influence of the splitter plate leading-edge geometry and the geometry of the shroud beneath the plate. (The shroud refers to the fairing beneath the plate that shields the wing mounting struts from the flow and prevents this flow from interfering with force-balance measurements.) Figure 25 shows a sketch of a wing mounted on a splitter plate in the wind tunnel. The second set of experiments, referred to as the Circular Splitter Plate Experiments, investigated the influence of the tunnel-floor boundary layer on the splitter plate. All experiments were done with no wing in the tunnel.

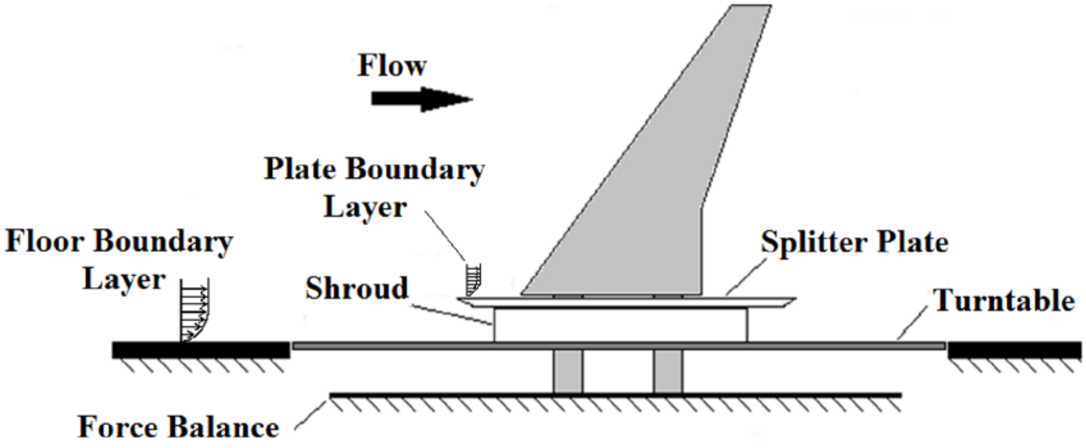

Figure 25. Sketch of a wing mounted on a splitter plate

5.8.1 Variable Geometry Splitter Plate Experiment

The results of the splitter plate experiments performed at UIUC have been documented in an American Institute of Aeronautics and Astronautics (AIAA) paper [34] and will be briefly discussed here. The first set of experiments investigated the effect of splitter-plate geometry on the flow over the splitter plate. Figure 26 shows a schematic of the variable geometry splitter plate used for this series of experiments. The splitter plate was divided into three separate components: the leading-edge section, the central section, and the trailing-edge section. These three sections were mounted on top of a streamlined shroud. The splitter plate contained three rows of streamwise pressure taps, which are also shown in figure 26. The setup was designed so that each part of the plate and the shroud could be removed and replaced with a different geometry.

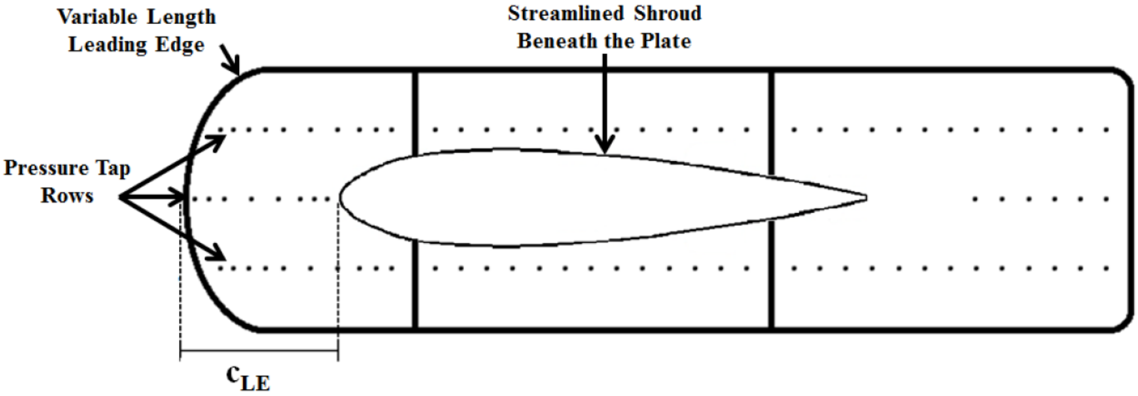

Figure 26. Variable geometry splitter plate

The two investigated geometric features of the splitter-plate leading edge were the streamwise length (c_{LE} defined in figure 26) and the streamwise profile, which will be described in the next paragraph. The thickness of the airfoil shroud beneath the plate was also investigated. The streamwise length of the plate leading edge, c_{LE}, was measured from the leading edge of the plate to the leading edge of the shroud beneath the plate, as shown in figure 26. Five different leading-edge lengths were tested and are shown in figure 27. The designations shown in figure 27 refer to the length of the component in approximate percentage of the length of the shroud. For example, c_{LE} of the component LE_5 was approximately 5% of the shroud length. Table 6 lists the values of c_{LE} and the actual percentage of the shroud length. The shroud was 11.85 in. long and 1.6 in. high, measured from the tunnel floor. The thickness of the splitter plate was 0.125 in.; therefore, the surface of the plate was 1.725 in. above the tunnel floor. The splitter plate was 4.82 in. wide.

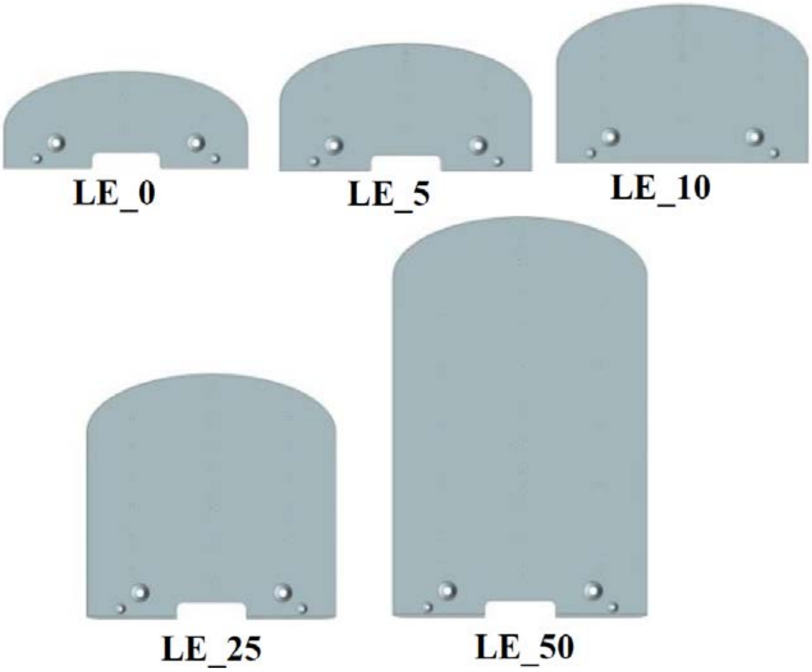

Figure 27. Leading-edge geometries used for variable geometry splitter plate; the designation for each component is explained in the text and table 6.

Table 6. Designations and sizes of the five leading-edge components

Leading-Edge Designations	c_{LE} (inches)	Actual % of Shroud Length
LE_0	0	0
LE_5	0.567	4.78
LE_10	1.134	9.56
LE_25	2.835	23.92
LE_50	5.67	47.85

The influence of the streamwise profile of the leading-edge component was also investigated. The primary profile that was tested will be referred to as the tapered profile and is shown in the top of figure 28. The tapered profile had a tip radius of 0.01 in., and the length of the tapered section was 0.4 in. This profile was used for all five leading-edge components shown in figure 27 and was used along the entire edge of the plate. If the flow is parallel to the plate, the tapered profile should cause only a small disturbance in the flow. A streamlined profile, shown at the bottom of figure 28, was also tested for the 25% length component and was designated LE_25A. The streamlined profile used the leading-edge geometry of a NACA 0012 airfoil. The length of the airfoil section was chosen so that the maximum thickness of the airfoil matched the constant thickness of the splitter plate. This resulted in a smooth transition from the NACA 0012 profile to the constant thickness of the plate. The streamlined profile was used only for the LE_25A component; the edges of the central and trailing-edge sections of the plate still had the tapered profile. As mentioned above, the constant thickness section of both profiles was 0.125 in.

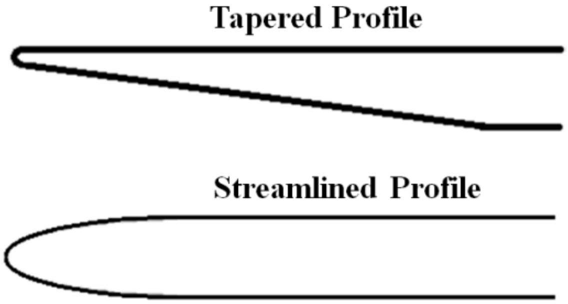

Figure 28. Streamwise profiles of variable geometry splitter-plate leading edge

In addition to the length and streamwise profile of the plate, the effect of shroud thickness was also investigated. (The shroud is the structure beneath the splitter plate that supports the splitter plate and shields the mounting struts of the wing from the flow.) The shroud profile was a symmetrical airfoil with a chord of 11.85 in. Two different thicknesses were tested, and the airfoil profiles used were a NACA 0014 and NACA 0024.

Figure 29 shows surface oil flow along the five leading-edge components from figure 27. For these results, the NACA 0012 shroud and tapered streamwise profile were used. The tunnel was set to a freestream velocity of 170 ft/s, which corresponded to $RE/ft = 1.03x10^6/ft$, and the shroud was at 0^o angle of attack. The red dashed line indicates the streamwise position of the shroud leading edge beneath the plate. Note that the images are to scale, and flow is from top to bottom. The large, dark, circular objects in the image are screwheads. The oil-flow images clearly show the presence of a 3D recirculation region near the leading edge of the plate. The separated region was highly 3D because of the relatively low aspect ratio of the splitter plates and the spanwise curvature of the leading edges. Although not shown here, surface-pressure measurements indicated a region of low pressure along the centerline of the plate beneath the separated flow. An important observation from these oil-flow images was that as the length of the leading-edge component decreased, the size of the separated region increased.

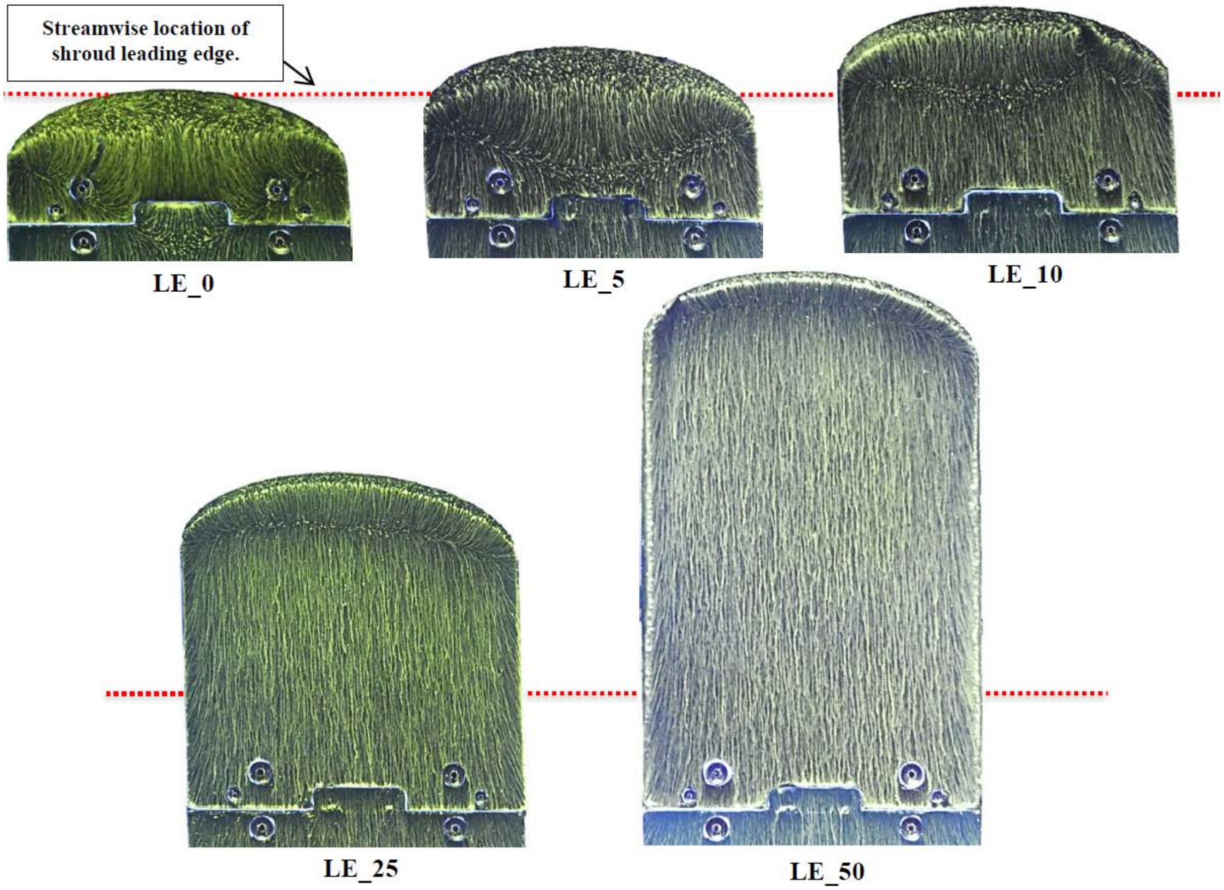

LE_0 LE_5 LE_10 LE_25 LE_50

Figure 29. Surface oil flow images for the five different leading edges of the variable geometry splitter plate. Red dashed line indicates location of the shroud leading edge beneath the plate. Flow is from top to bottom (A = 0º, Re/FT = 1.03X106/FT tapered).

The separated flow indicates that the leading edge of the splitter plate was at an angle of attack relative to the local flow. The plate was mounted such that it was parallel to the floor and, therefore, it was also parallel to the freestream. The angle of attack of the plate leading edge was a result of the flow being deflected because of the blockage of the plate and shroud. The flow under the plate was restricted by the shroud and the growing boundary layers on the tunnel floor and the underside of the splitter plate. The flow was deflected in three dimensions, resulting in a local angle of attack at the plate leading edge and the flow separated at the sharp point of the tapered profile shown in figure 28. The effect is shown in figure 30. This explanation is also consistent with the observation of an increase in the size of the separated region as the leading-edge length was reduced. As the length of the leading-edge component was reduced, the leading edge of the splitter plate moved closer to the shroud. The flow deflection resulting from the presence of the shroud should be largest near the shroud; as the leading-edge length is reduced, the local angle of attack should increase, resulting in a larger separation region.

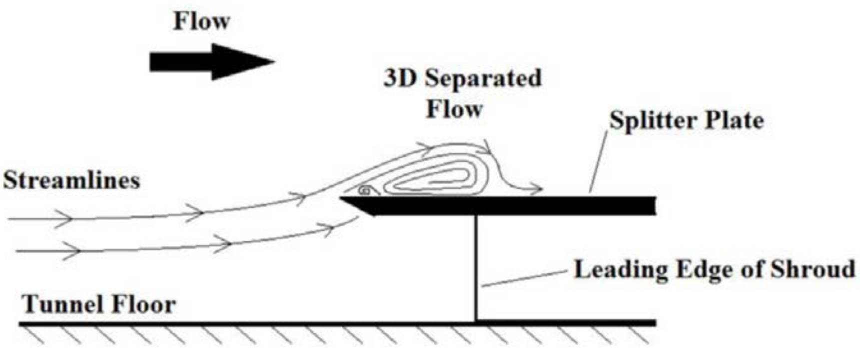

Figure 30. Flow separated at the leading edge of the splitter plates

The relatively sharp point of the tapered streamwise profile was assumed to be a major factor in the formation of the separated flow along the splitter-plate leading edge. This was verified by testing the streamlined profile shown in figure 28. The length of the component with the streamlined profile matched the length of the LE_25 component and will be referred to as LE_25A. Figure 31 compares the surface oil flow for the tapered profile and streamlined profile for the same conditions as figure 29. In figure 31, no oil flow was captured on the airfoil section of the leading edge, only the flat surface of the plate. The image is cropped to show only the oil. The large recirculation region on LE_25 is not observed in LE_25A, indicating that the streamlined NACA 0012 leading edge did not have a large region of separated flow despite being in the same flow conditions as LE_25. It is possible that separation may have occurred on the curved section of the leading edge; however, with no oil flow or pressure measurements in that location, it was not possible to verify. The results do show that even if separation was still occurring, the streamwise extent of this separation was significantly reduced as a result of using the streamlined profile. This has important implications for the design of future splitter plates if leading-edge separation is to be avoided.

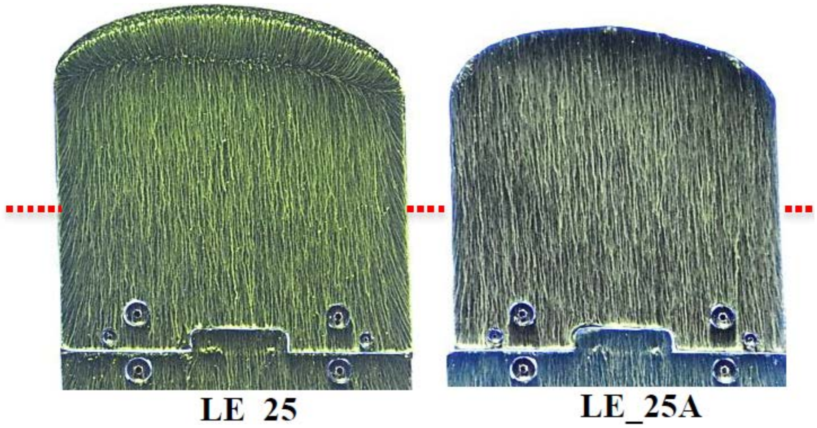

Figure 31. Oilflow comparison of LE_25 and LE_25A; dashed red line indicates location of shroud leading edge; flow is from top to bottom (A = 0º, Re/FT = 1.03X106/FT), NACA 0014 shroud

Figure 32 shows the influence of shroud thickness on the streamwise pressure distributions on LE_10 and LE_25 for the same flow conditions as above. For both leading-edge lengths the low-pressure region grew when the thicker shroud was used, but the effect was more pronounced for the shorter leading-edge component LE_10. These trends were observed for the other three leading-edge lengths. The low-pressure region is beneath the separated flow. The results of figure 32 are consistent with the idea that the leading-edge separation was a result of blockage beneath the plate, which deflects the flow and results in the leading edge of the plate being at an angle of attack relative to the local flow. As the thickness of the shroud increased, the amount of blockage increased, resulting in more deflection and a larger local angle of attack. When the leading-edge component was longer (i.e., larger c_{LE}), the effect was less pronounced because the amount of flow deflection decreases farther away from the shroud.

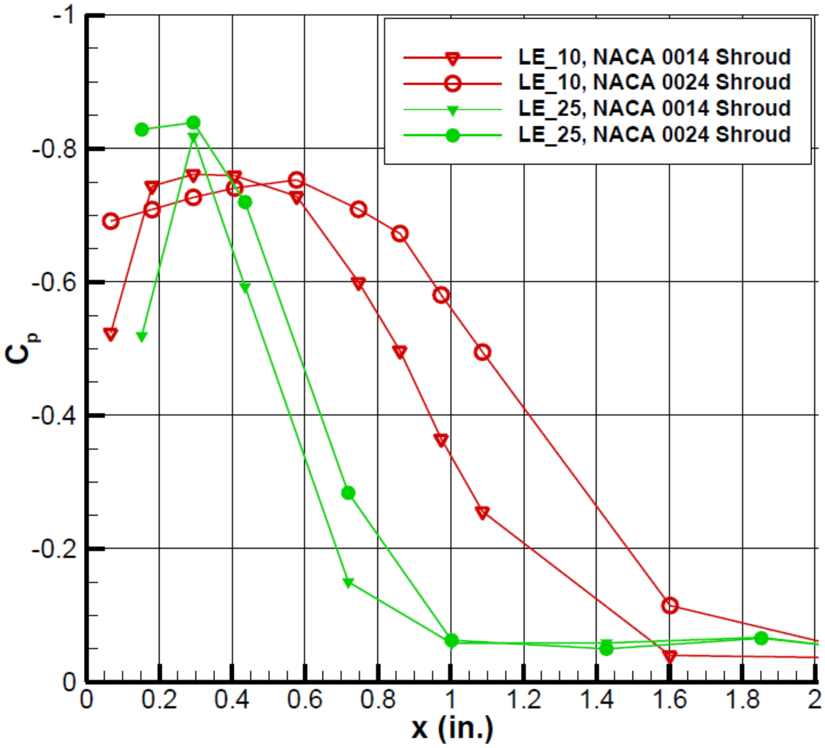

Figure 32. Effect of shroud thickness on centerline pressure for LE_10 and LE_25 (A = 0º, Re/FT = 1.03X106/FT); tapered streamwise profile

5.8.2 Circular Splitter-Plate Experiments

A second set of experiments used a different splitter-plate geometry and a tunnel-floor boundary-layer suction/blowing system to study the effects of the floor boundary-layer thickness on the flow over the splitter plate. The splitter plate used for these experiments was substantially different from the variable geometry splitter plate previously discussed. This splitter plate, which will be referred to as the "circular splitter plate," was a flat disk with a diameter of 25.73 in. and a thickness of 0.25 in. A cylindrical shroud with a diameter of 6 in. was used. The shroud was 1.6 in. high, so the surface of the splitter plate was 1.85 in. above the tunnel floor. The streamwise profile of this plate was a hemisphere with a radius of 0.125 in., which extended along the entire circumference of the plate. Figure 33 shows an image of the splitter plate mounted on the tunnel floor and the holes used for boundary-layer suction/blowing.

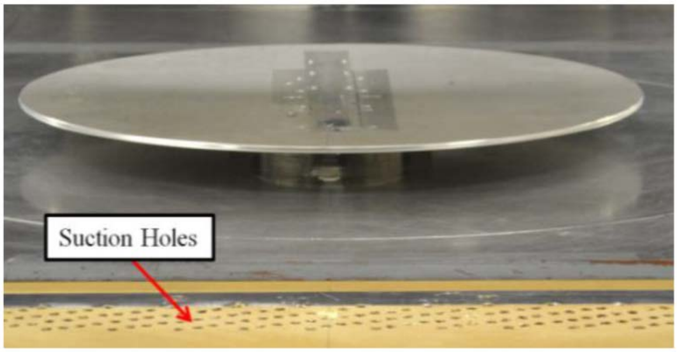

Figure 33. Circular splitter plate mounted in the wind tunnel with holes used for boundary-layer suction/blowing shown

A boundary-layer suction/blowing system was developed upstream of the plate. The system was capable of decreasing or increasing the boundary-layer height by approximately 60%.

The results from this set of experiments will briefly be discussed here; more detail can be found in Diebold et al. [34]. Boundary-layer measurements were made on the tunnel floor and on the surface of the splitter plate. The suction/blowing system was used to modify the boundary layer on the tunnel floor, and the change in the splitter plate boundary layer was measured. The results of the boundary-layer measurements are summarized in tables 7 and 8. Table 7 shows the boundary-layer height on the tunnel floor when there was no change to the floor boundary layer and when suction or blowing was applied. Table 8 shows the boundary-layer heights on the splitter plate for the three different tunnel-floor boundary-layer cases. The boundary-layer thickness δ_{99} was defined by $U/U_\infty = 0.99$. The application of suction decreased the floor boundary-layer thickness by 58%, whereas blowing increased it by 58%. Despite the large changes in the tunnel-floor boundary layer, the splitter-plate boundary layer was relatively unaffected. The application of suction and blowing to the tunnel floor resulted in a change of +14% and -18% to the splitter-plate boundary layer, respectively.

Table 7. Tunnel-floor boundary-layer thickness for three different floor boundary-layer modification methods

Boundary Layer Modification	δ_{99} (inches)
None	1.016
Suction	0.424
Blowing	1.615

Table 8. Circular splitter-plate boundary-layer thickness for three different floor boundary-layer modification methods (plate on cylindrical shroud)

Boundary-Layer Modification	δ_{99} (inches)
None	0.316
Suction	0.360
Blowing	0.373

Overall, the flow over the circular splitter plate was not significantly influenced by the state of the tunnel-floor boundary layer. This highlights a potential benefit of a splitter plate. By mounting a wing on a splitter plate, it is possible to reduce the influence of a specific tunnel-floor boundary layer. This may be used to improve comparisons between similar models tested in different tunnels and comparisons between experiments and CFD.

5.8.3 Splitter-Plate Design Guidelines

The goal of the splitter plate experiments was to develop a set of guidelines that can be used in the design of future splitter plates and, especially, the splitter plates for the low-to-medium and high-Reynolds number tests to follow in the Swept-Wing Icing Program. The results of the wind-tunnel experiments suggest the following set of splitter-plate design guidelines. (It should be noted that not all of the experimental results were discussed in this report. For results showing the influence of angle of attack and the location and shape of the shroud beneath the circular plate, see Diebold et al. [34].)

1. Extending the splitter plate a short distance upstream of the model does not necessarily guarantee a thin boundary layer in the vicinity of the model. Care must be taken to either reduce the blockage beneath the plate or design the leading edge to minimize flow separation.

2. The influence of blockage beneath the plate can be reduced by a thin streamlined shroud, or by placing the shroud far downstream of the leading edge of the plate.

3. Proper design of the streamwise profile of the leading edge (see figures 28 and 31) can also be used to reduce separation. Because of the likelihood of the leading edge of the plate being at a local angle of attack because of blockage, a sharp tapered streamwise profile is not ideal, and a rounded leading edge, less sensitive to angle of attack, is preferable.

4. If experiments will be conducted at large angles of attack, an axisymmetric splitter plate and shroud will minimize the influence of angle of attack on the flow over a splitter plate. Angle of attack effects will also be reduced by placing the shroud far downstream of the leading edge of the plate. It may also be beneficial to keep the shroud and plate fixed while the model rotates independently of the splitter plate. A low aspect ratio splitter plate is not recommended for tests at large angles of attack.

5.8.4 Splitter-Plate Geometry for 7X10 and F1 Wind-Tunnel Testing

The guidelines discussed above were used to design a splitter plate for use in the low-to-medium Reynolds number 7-by-10 wind-tunnel tests and will be used for design of the splitter plate for the high-Reynolds number F1 wind-tunnel tests. The design selected was a circular splitter plate with a streamlined shroud. For the low-to-medium Reynolds number 7-by-10 tests, the circular plate has a diameter of 52.3 in. and is 0.5 in. thick. The leading-edge streamwise profile is circular with a radius of 0.25 in. A circular streamwise profile was selected for manufacturing simplicity and to reduce the amount of flow separation along the leading edge. The shroud beneath the plate was a NACA 0018 airfoil with a chord of 25.0 in. and a maximum thickness of 4.5 in. The surface of the plate was 2.4 in. above the tunnel floor. This height was selected to ensure the surface of the plate was outside of the tunnel-floor boundary layer. This geometry will be scaled up for the high-Reynolds number F1 tests.

6. DIGITALLY GENERATED ICE SHAPES

A large number and variety of ice shapes have been accreted during the IRT tests on the inboard, midspan, and outboard sections of the CRM wing. Because of the size constraints and cloud properties in the IRT, only ice accretions on 1–2 ft spanwise sections at the three span locations of the ice accretions were laser scanned and then post-processed digitally [35].

High-fidelity artificial ice shapes maintain the highly detailed, 3D characteristics and roughness of the original ice accretion. Artificial ice shapes created directly from accretions on icing tunnel models are referred to as high-fidelity ice shapes. High-fidelity ice shapes maintain the highly detailed, 3D characteristics and roughness of the original ice accretion. Currently, two methods are used to create these high-fidelity ice shapes: 1) digital scanning followed by rapid prototyping or 2) creating molds of the ice shapes and then creating casts from the molds. For the Swept-Wing Icing Project, the scanning/rapid prototyping method has been chosen. An example of a scanned high-fidelity ice shape is shown in figure 34. This would then be used in the rapid prototyping method to create the artificial ice shape.

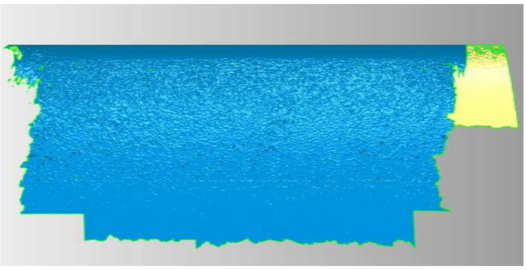

Figure 34. High-fidelity ice shape

The high-fidelity scans are post-processed in Geomagic Studio®. Geomagic Studio is a program that processes and manipulates both point cloud datasets created by laser scanners and surfaces created in computer-aided design (CAD) programs. From the laser scan, a large number of individual data points are imported into Geomagic Studio, in which solid surfaces are created between adjacent data points. For more complex ice shapes, there are many holes that must be manually filled in to generate an ice shape. A part of a scanned ice shape that requires repairs is shown in figure 35. For the scanned shapes to be used to generate rapid prototyped ice shapes, they must be edited to create a single, continuous surface. Each individual hole is filled in by using a series of tools in Geomagic Studio, which can create bridges between two surfaces and estimate how holes should be filled. The process of filling in a single section using these tools is shown in figure 36. The first step shows the bridges created to connect two separate surfaces; the second step shows the estimation by Geomagic Studio of how a hole should be filled; and the third step depicts the final connected surfaces. The user creates the bridges and Geomagic proposes how to fill the hole. If the user is satisfied and accepts the proposal, this becomes the final connected surface. If not, the user starts over, creating different bridges.

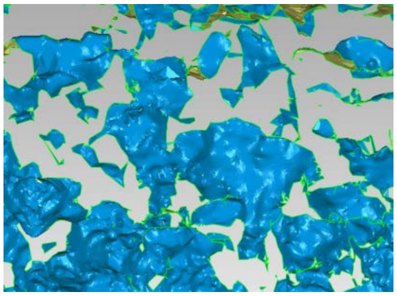

Figure 35. Ice-shape surface before repair

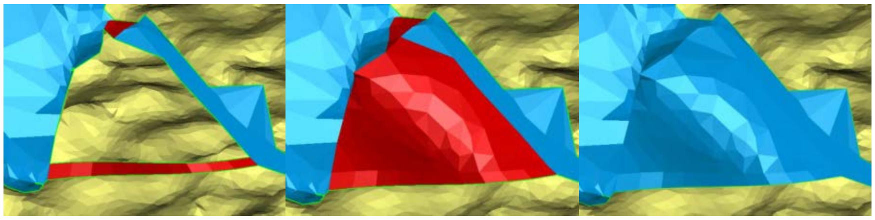

Figure 36. Ice-shape repair process using Geomagic Studio

After all the holes have been filled to create a single surface, the surface can either be exported to a CAD program or used in the morphing process**.**

Low-fidelity artificial ice shapes do not possess the highly detailed, 3D characteristics and roughness of natural or tunnel ice accretions. They possess only major geometric features, which may be sufficient to reproduce important aerodynamic effects. Low-fidelity artificial ice shapes may be created from high-fidelity ones by applying methods to eliminate small-scale features, or they may be created directly from computer simulations. An example of a low-fidelity artificial ice shape model that maintains the horn height found in the high-fidelity model without including its detailed roughness is shown in figure 37. Both high- and low-fidelity artificial ice shapes will be used in future aerodynamic wind-tunnel entries.

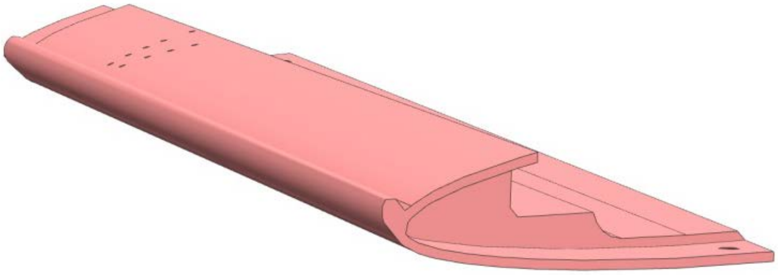

Figure 37. Low-fidelity ice shape

Although three spanwise stations of the CRM are being tested in the IRT, this accounts for only a small fraction of the entire leading edge of the swept wing. The ice accretions between these locations are also extremely important to the effect on the aerodynamic properties of the whole wing. Geomagic Studio was used to develop a method to generate full-scale and full-span ice shapes using these limited data for a wing with specified taper and twist. This method involves an averaging, or morphing, process that is applied to two separate high-fidelity ice shapes to create a single full-scale leading-edge ice shape between the two sections.

Before the morphing process can be applied, the 1–2 ft spanwise scanned ice shapes must be trimmed to a length that preserves specific defining features, such as a single full scallop. When morphing between two stations, a linear weighting process is applied to the two trimmed ice shapes on each end to create a series of trimmed ice shapes with geometries that fall between the two original ice shape geometries. The first scanned ice shape, which is a rime ice shape in figure 38, is 100% ice shape 1 and 0% ice shape 2; the second scanned ice shape, which is a scalloped ice shape in figure 38, is 0% ice shape 1 and 100% ice shape 2. The other ice shapes created to represent shapes between the two using the linear weighting process fall at various percentages between ice shapes 1 and 2. For example, an ice shape between ice shapes 1 and 2 might be 75% ice shape 1 and 25% ice shape 2 at a location 25% of the way from ice shape 1 to ice shape 2.

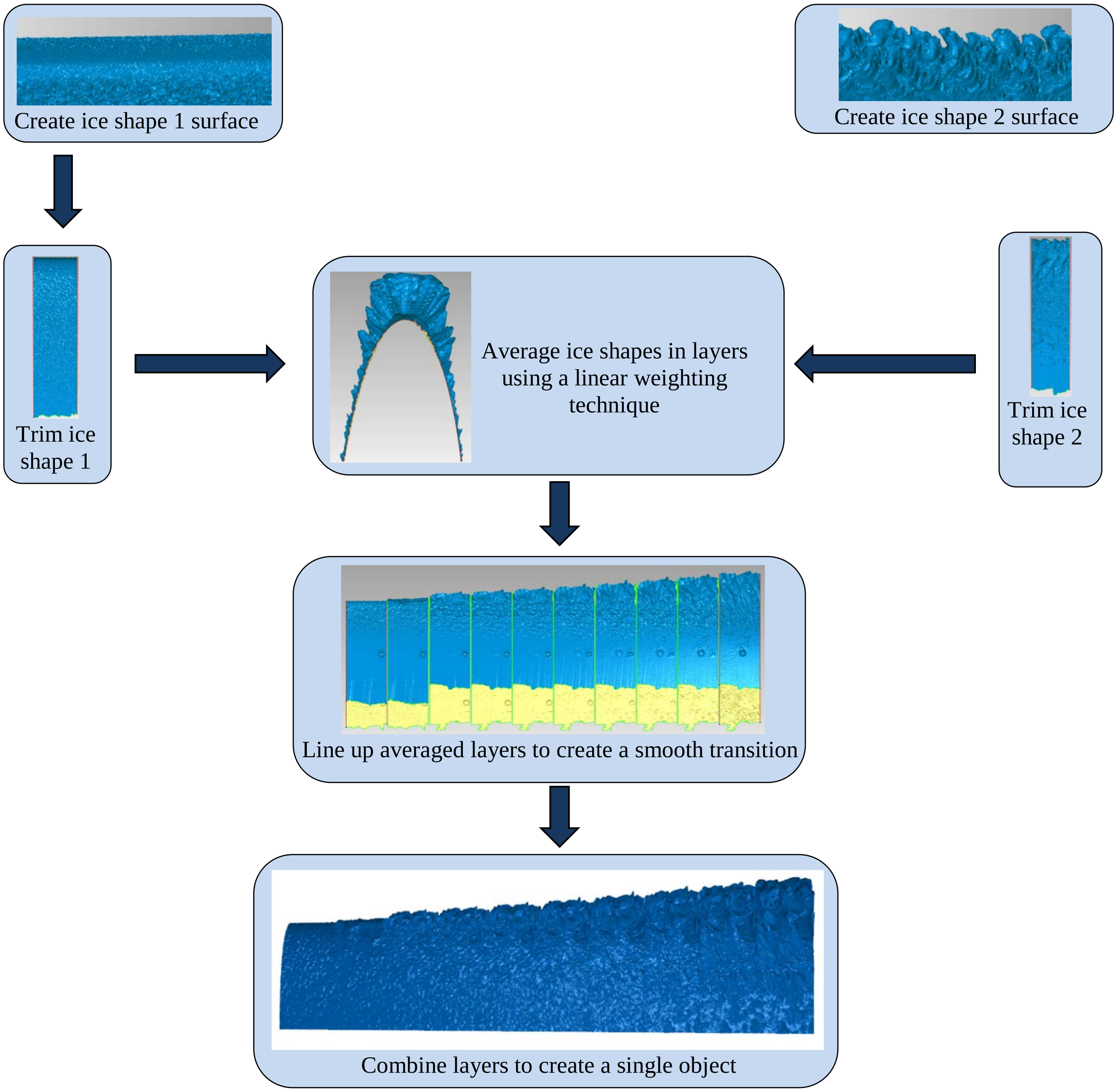

Figure 38. Method to generate full-scale ice shapes over a defined span

To generate the ice shapes in the linear weighting process, the built-in average function in Geomagic Studio is used. To achieve specific weighted percentages for a new, averaged ice shape, copies of the ice shape are created to produce the weighting. Creating the ice shape that is closer in geometry to ice shape 1 in the example above may require averaging three copies of ice shape 1 and one copy of ice shape 2, depending on the geometries of ice shapes 1 and 2. This process is repeated using the appropriate weights until there are enough trimmed ice-shape sections to create a smooth transition between the two original ice shapes.

Because the inboard and outboard models tested in the IRT do not represent the root and tip geometries of the 65% CRM wing, the ice shapes between the outboard section and the wing tip and the inboard section and the wing root must be extrapolated from the existing data. This extrapolation process will use LEWICE3D simulation results to help guide the ice shape creation. Specifics of the extrapolation method are still being developed.

Because each averaged ice-shape section was created separately, there will be small gaps between each of the trimmed pieces when they are placed together to create a full-span leading-edge ice shape. To place the new ice shape on the leading-edge of a wing, these gaps must be filled in to create a single, solid shape. This is done using the same method previously used to repair holes in the scanned ice shapes. This method will be applied over the length of the full-scale leading edge of the 65% CRM using the high-fidelity ice shapes from the inboard, midspan, and outboard wind-tunnel entries in the IRT.

An example of an application of these methods is shown in figure 38 using a rime shape and a scalloped shape. In some cases, smaller ice accretions, such as the rime ice, will form near the root of the leading edge of the wing, whereas larger ice accretions, such as the scalloped ice, will form near the tip of the leading edge of the wing.

After the high-fidelity ice shapes have been edited to create full-span leading-edge ice shapes, low-fidelity versions of these shapes will be created for a planned total of approximately 39 leading-edge ice shapes to be tested in the low-to-medium Reynold’s number entries in the 7-by-10 wind tunnel. From these iced leading edges, approximately 18 shapes will be selected for the high-Reynold’s number entries in the F1 wind tunnel. The majority of these shapes will be constructed using rapid prototype methods, whereas some of the low-fidelity shapes may be constructed through alternate means. Realize Inc. specializes in SLA and uses an iPro™ 9000 SLA® Center, which can obtain accuracies that rival those of computer numerical control machined parts. This supplier and process, or something similar, will be used to produce the high-fidelity and most of the low-fidelity ice shapes. The removable leading edges created for the 7-by-10 wind tunnel model will be generated in two separate spanwise pieces, whereas the removable leading edges created for the F1 wind-tunnel model will be generated in three separate spanwise pieces because of the size limitations of the rapid prototyping machines. In addition, creating these removable leading edges in multiple parts ensures that they are less subject to warping when not in use.

7. SUMMARY AND CONCLUSIONS

This report summarizes the results of the research conducted at the University of Illinois as part of a grant with the goal of improving our understanding of iced swept-wing aerodynamics and developing experimental techniques for experimental study. The main results of this work are summarized as follows:

- Development of an ice shape classification system for swept wings, based on the aerodynamics and flowfield of the ice accretion.
- The classification categories are roughness, streamwise ice, spanwise ridge ice, and horn ice. The horn ice category requires a subcategory of nominally 3D and highly 3D, the latter reflecting the presence of scallops.

- To generate high-fidelity artificial ice shapes for use in aerodynamic tests, it is necessary to have a method to reliably capture the detailed geometry of an ice accretion in an icing wind tunnel. In the past, the method used has been a mold and casting technique. NASA's Glenn Research Center has developed a new laser-scanning method that creates an accurate digital representation of the ice accretion. The test model is constructed using rapid prototype manufacturing techniques.
- This laser scanner and rapid prototyping process has been validated at the University of Illinois by comparing the aerodynamic impact resulting from the scanned ice shapes and ice-shape castings. The baseline geometry selected for the swept-wing icing program is a 65% scale common research model (CRM), designated CRM65.
- A series of aerodynamic tests have been carried out at the University of Illinois, measuring the performance degradation of a swept wing due to a simple ice shape simulation on a swept-wing model.
- During these wind-tunnel tests, the complex flowfield behind horn ice on a swept wing was extensively studied. The tests were conducted at very low Reynolds numbers, and it is unclear if the results observed will be representative of wings at higher Reynolds numbers. Therefore, higher Reynolds number testing is needed.
- One of the primary goals of the low-Reynolds number testing at the University of Illinois was to investigate the use of various techniques for examining the flowfield and aerodynamics for an iced and clean swept wing. The advanced techniques that received the most attention include PSP and 5HP wake surveys.
- Although PSP is potentially a useful tool, it has been determined that other measurements will be more valuable within the constrained aerodynamic wind-tunnel schedules for the low-to-medium and high-Reynolds number testing.
- The 5HP wake survey has demonstrated significant potential for improving our understanding of the flowfield and aerodynamics of swept wings. The measurements of pressure and velocity are used to determine the total lift and drag on the model, resolve the spanwise distributions of the loads, and decompose the drag into profile and induced drag components.
- The wake surveys have shown that the horn ice resulted in a significant increase in profile drag, whereas the induced drag was virtually unaffected for a given C_L. This increase in profile drag resulted from the separated flowfield behind the horn ice.
- As the angle of attack increased, the profile drag of the ice wing increased rapidly because of the growth of the leading-edge vortex observed in the surface oil flow.
- The wake survey technique showed local peaks in the spanwise distribution of the drag coefficient, and these peaks were linked to areas along the span in which the leading-edge vortex was larger than neighboring spanwise locations.
- The experimental icing data acquired for this program will use a semispan swept-wing model. To reduce the influence of the tunnel-floor boundary layer, it has been decided that the semispan swept-wing model will be mounted to a splitter plate.
- A series of experiments at the University of Illinois has been performed to develop splitter-plate design guidelines. These experiments studied how the flow over the splitter plate was influenced by the geometry of the splitter plate.
- Design guidelines were developed from these tests, and these guidelines are being followed to design a splitter plate for the 7-by-10 and F1 wind-tunnel campaigns.

- A methodology has been developed with the leadership of NASA's Glenn Research Center to develop 3D full semispan artificial ice shapes from laser-scanned ice shapes at three small sections along the wingspan.

The work completed during this grant represents critical progress toward the goal of obtaining high-Reynolds number experimental data for swept wings with ice. The work done so far will be used to prepare for and maximize our productivity in the 7-by-10 and F1 wind tunnel tests and to ensure that we are performing experiments that will contribute to our understanding of swept-wing icing.

8. REFERENCES

1. Bragg, M.B., Broeren, A.P., and Blumenthal, L.A. (2005). Iced-Airfoil Aerodynamics. *Progress in Aerospace Sciences, 41*(5), 323–418.

2. Lynch, F.T., Khodadoust, A., (2001). Effects of Ice Accretions on Aircraft Aerodynamics. *Progress in Aerospace Sciences, 37*(8), 669-76

3. Busch, G.T., Bragg, M.B. (2009). *Experimental Study of Full-Scale Iced-Airfoil Aerodynamic Performance using Sub-Scale Simulations*. (AIAA 2009-4264).

4. Broeren, A.P., Bragg, M.B., Addy, H.E., Lee, S., Moens, F., Guffond, D. (2010). Effect of High-Fidelity Ice-Accretion Simulations on Full-Scale Airfoil Performance. *Journal of Aircraft, 47*(1), 240–254.

5. Khodadoust, A., Bragg, M.B. (1995). Aerodynamics of a Finite Swept Wing with Simulated Ice. *Journal of Aircraft, 32*(1), 137–144.

6. Bragg, M.B., Kerho, M.F., Khodadoust, A. (1993). *LDV Flowfield Measurements on a Straight and Swept Wing with a Simulated Ice Accretion*, (AIAA 1993-0300).

7. Papadakis, M., Yeong, H.W., Wong, S.C. (2003). *Aerodynamic Performance of a Swept Wing with Ice Accretions.* (AIAA 2003-0731).

8. Papadakis, M., Yeong, H.W., Wong, S.C. (2004). *Aerodynamic Performance of a Swept Wing with Simulated Ice Shapes*. (AIAA 2004-0734).

9. NASA Report. (2013). Aerodynamic Classification of Swept-Wing Ice Accretion. (NASA/TM – 2013-216381).

10. Diebold, J.M., Broeren, A.P, Bragg, M.B. (2013). *Aerodynamic Classification of Swept-Wing Ice Accretion*. Paper presented at the 5th AIAA Atmospheric and Space Environments Conference, San Diego, CA. (AIAA Paper 2013-2825).

11. Vargas, M. (2007). Current Experimental Basis for Modeling Ice Accretions on Swept Wings. *Journal of Aircraft, 44*(1), 274–290.

12. Papadakis, M., Yeong, H.W., Wong, S.C., Vargas, M., Potapczuk, M.G. (2003). *Aerodynamic Performance of a Swept Wing with Ice Accretions*. Paper presented at the 41st Aerospace Sciences Meeting and Exhibit, Reno NV. (AIAA Paper 2003-0731).

13. NASA Report. (2011). Aerodynamic Simulation of Ice Accretion on Airfoils. (NASA/TP—2001-216929).

14. NASA Report. (1987). New Methods and Materials for Molding and Casting Ice Formations. (NASA TM 100126).

15. Fujiwara, G.E.C, Wiberg, B.D., Woodards, B.S., Bragg, M.B. (2014). *3D Swept Hybrid Wing Design Method for Icing Wind Tunnel Tests*. (AIAA 2014-2616).

16. Lee, S., Broeren, A.P., Kreeger, R.E., Potapczuk, M., Utt, L. (2014). *Implementation and Validation of 3D Ice Accretion Measurement Methodology*. (AIAA 2014-2613).

17. Broeren, A.P., Addy, H.E., Lee, S., Monastero, M.C. (2014). Validation of 3D Ice Accretion Measurement Methodology for Experimental Aerodynamic Simulation. (AIAA 2014-2614).

18. Monastero, M.C., Bragg, M.B. (2014). *Validation of 3D Ice Accretion Measurement Methodology Using Pressure-Sensitive Paint*. (AIAA 2014-2615).

19. Vassberg, J.C., DeHann, M.A., Rivers, S.M., Wahls, R.A. (2008). *Development of a Common Research Model for Applied CFD Validation Studies*. Paper presented at the 26th AIAA Applied Aerodynamics Conference, Honolulu, HI. (AIAA Paper 2008-6919).

20. Diebold, J.M. (2012). *Aerodynamics of a Swept Wing with Leading-Edge Ice at Low Reynolds Number* (M.S. Thesis). Department of Aeronautical and Astronautical Engineering, University of Illinois, Urbana, IL.

21. Diebold, J.M., Monastero, M.C., Bragg, M.B. (2012). *Aerodynamic of a Swept Wing with Ice Accretion at Low Reynolds Number*. (AIAA 2012-2795).

22. Liu, T., Sullivan, J.P. (2005). *Pressure and temperature sensitive paints*, Heidelberg, Germany: Springer-Verlag.

23. Brune, G. W. (1994). Quantitative Low Speed Wake Surveys. *Journal of Aircraft, 31*(2), 249–255.

24. Diebold, J.M., Bragg, M.B. (2013). *Study of a Swept Wing with Leading-Edge Ice Using a Wake Survey Technique*. (AIAA 2013-0245).

25. Diebold, J.M., Bragg, M.B., “Wake-Survey Technique for Iced Swept-Wing Aerodynamics,” To be published as an *AIAA Journal* Technical Note in 2015.

26. Lu, B., Bragg, M. B. (2003). *Airfoil Drag Measurement with Simulated Leading-Edge Ice Using the Wake Survey Method*. (AIAA 2003-1094).

27. Gatlin, G. M., McGhee, R. J. (1997). Experimental Investigation of Semispan Model Testing Techniques. *Journal of Aircraft*, *34*(4), 500–505.

28. AGARD Report. (1959). Notes on Half model testing in wind tunnels. (Volume 298).

29. Malik, A., Render, P.M. (2010). *Use of Wall Suction in Half Model Wind Tunnel Testing*. Paper presented at the 28th AIAA Applied Aerodynamics Conference. (AIAA Paper 2010-4828).

30. Gand, F., Brunet, B., Deck, S. (2012). Experimental and Numerical Investigation of a Wing-Body Junction Flow. *AIAA Journal*, *50*(12), 2711–2719.

31. NASA Report. (1996). Computational Analysis of Semispan Model Test Techniques. (NASA CR 4709).

32. Wells, S.L. (1992). *The Effect of Sidewall Suction on the Aerodynamics of a Semispan Wing with Simulated Ice*. M.S. Thesis Department of Aeronautical and Astronautical Engineering, University of Illinois, Urbana, IL.

33. Giguere, P., Selig, M. S. (1997). Freestream Velocity Corrections for Two-Dimensional Testing with Splitter Plates. *AIAA Journal*, *35*(7), 1195–1200.

34. Diebold, J.M, Woodard, B.S., Monastero, M.C., Bragg, M.B. (2015). *Experimental Study of Splitter Plates for Use with Semispan Wing Models*. (AIAA 2015-1227).

35. NASA Report. (2012). Development of 3-D Ice Accretion Measurement Method. (NASA/TM-2012-217702).